Journal of Volcanology and Geothermal Research 420 (2021) 107381

Contents lists available at ScienceDirect

Journal of Volcanology and Geothermal Research

journal homepage: www.elsevier.com/locate/jvolgeores

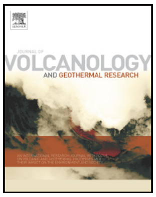

Evaluating the state-of-the-art in remote volcanic eruption characterization Part II: Ulawun volcano, Papua New Guinea

Kathleen McKee[a,*,1], Cassandra M. Smith[b], Kevin Reath[c], Eveanjelene Snee[d], Sean Maher[e], Robin S. Matoza[e], Simon Carn[f], Diana C. Roman[a], Larry Mastin[g], Kyle Anderson[h], David Damby[h], Ima Itikarai[i], Kila Mulina[i], Steve Saunders[i], Jelle D. Assink[j], Rodrigo de Negri Leiva[e,k], Anna Perttu[l]

[a] *Earth and Planets Laboratory, Carnegie Institution for Science, Washington, DC, USA*
[b] *Alaska Volcano Observatory, U.S. Geological Survey, Anchorage, AK, USA*
[c] *Department of Earth and Atmospheric Sciences, Cornell University, Ithaca, NY, USA*
[d] *School of Earth and Environmental Sciences, Cardiff University, Cardiff, Wales, UK*
[e] *Department of Earth Science and Earth Research Institute, University of California, Santa Barbara, Santa Barbara, CA, USA*
[f] *Department of Geological and Mining Engineering and Sciences, Michigan Technological University, Houghton, MI, USA*
[g] *U.S. Geological Survey Cascades Volcano Observatory, Vancouver, WA, USA*
[h] *U.S. Geological Survey, California Volcano Observatory, Moffett Field, CA, USA*
[i] *Rabaul Volcano Observatory, Department of Mining and Petroleum, Geological Survey of Papua New Guinea, Rabaul, Papua New Guinea*
[j] *R&D Seismology and Acoustics, Royal Netherlands Meteorological Institute (KNMI), De Bilt, Netherlands*
[k] *NDC-CTBT of the Chilean Nuclear Energy Commission, Chile*
[l] *Earth Observatory of Singapore, Nanyang Technological University, Singapore*

ARTICLE INFO

Article history:
Received 9 January 2021
Received in revised form 16 August 2021
Accepted 18 August 2021
Available online 20 August 2021

Keywords:
Volcanic eruption characterization
Satellite remote sensing
Infrasound
Lightning
Plume modeling
Ulawun volcano

ABSTRACT

Retrospective eruption characterization is valuable for advancing our understanding of volcanic systems and evaluating our observational capabilities, especially with remote technologies (defined here as a space-borne system or non-local, ground-based instrumentation which include regional and remote infrasound sensors). In June 2019, the open-system Ulawun volcano, Papua New Guinea, produced a VEI 4 eruption. We combined data from satellites (including Sentinel-2, TROPOMI, MODIS, Himawari-8), the International Monitoring System infrasound network, and GLD360 globally detected lightning with information from the local authorities and social media to characterize the pre-, *syn-* and post-eruptive behaviour. The Rabaul Volcano Observatory recorded ~24 h of seismicity and detected SO_2 emissions ~16 h before the visually-documented start of the Plinian phase on 26 June at 04:20 UTC. Infrasound and SO_2 detections suggest the eruption started during the night on 24 June 2019 at 10:39 UTC ~38 h before ash detections with a gas-dominated jetting phase. Local reports and infrasound detections show that the second phase of the eruption started on 25 June 19:28 UTC with ~6 h of jetting. The first detected lightning occurred on 26 June 00:14 UTC, and ash emissions were first detected by Himawari-8 at 01:00 UTC. Post-eruptive satellite imagery indicates new flow deposits to the south and north of the edifice and ash fall to the west and southwest. In particular, regional infrasound data provided novel insight into eruption onset and *syn*-eruptive changes in intensity. We conclude that, while remote observations are sufficient for detection and tracking of syn-eruptive changes, key challenges in data latency, acquisition, and synthesis must be addressed to improve future near-real-time characterization of eruptions at minimally-monitored or unmonitored volcanoes.

1. Introduction

Remote geophysical observations, which include satellite remote sensing, infrasound at 250 km or greater, and lightning detections, are often essential for detection and characterization of volcanic unrest and eruption. Data from these technologies can confirm subaerial activity, the presence, distribution, and quantity of ash, gas and aerosols, and show thermal output, deformation, and *syn*-eruptive activity changes (e.g., Fee and Matoza, 2013; Poland et al., 2020; and references therein). These data are complementary to observations from local, ground-based monitoring instrumentation and are critical when such data are not available. Combining data from remote tools has proven valuable for eruption characterization and for broadening our understanding of volcanic processes (e.g., Fee et al., 2010; Perttu et al., 2020; Van Eaton

---

* Corresponding author.
E-mail address: kfmckee@carnegiescience.edu (K. McKee).

[1] Now at Los Alamos National Laboratory, Los Alamos, NM, USA

https://doi.org/10.1016/j.jvolgeores.2021.107381

et al., 2020). Retrospective eruption characterization involves gathering available data and analyzing an eruptive sequence from quiescence or background activity through unrest, eruption and a return to quiescence or background. Such analyses serve to advance our understanding of volcanic processes and to enhance our ability to characterize eruptions when observations are limited.

Unrest is a "deviation from the background or baseline behaviour of a volcano towards a behaviour that is a cause for concern in the short term (hours to few months) because it might prelude an eruption." (Phillipson et al., 2013). Primary observations that indicate unrest at volcanoes include ground deformation, increase in thermal output, changes in outgassing, changes at a crater lake (e.g., color), and changes in seismicity (Phillipson et al., 2013), but are limited to the first four when using remote tools. With satellite remote sensing, we can detect outgassing and thermal output at open-system volcanoes, but often not deformation (Ebmeier et al., 2013), while for closed systems we can often detect deformation, but outgassing and thermal output are often low or not detectable (Reath et al., 2019a). A volcano is considered open if it has a permanent or semi-permanent open conduit or pathway for gas escape (Chaussard et al., 2013). From an observational perspective, this suggests a given open volcanic system will have near-continuous, measurable gas emission, be it passive or explosive. These include systems with open lava lakes (e.g., Kīlauea 2008–2018, Ambrym, Villarrica, Erebus, and Masaya volcanoes), persistent low-level eruptive activity (e.g. Sakurajima, Stromboli, and Yasur volcanoes), and persistent passive degassing (e.g., Ulawun) (Carn et al., 2017).

The start of an eruption is usually defined by the ejection of solid material (e.g. ash/tephra and lava) from the vent. Knowing when ash, tephra, or lava are ejected is critical as these pose a threat to local communities and air traffic. This definition does not distinguish between the eruption start time and the detection time. With a local monitoring network, the detection time and eruption start time are often the same or similar. With remote data, the eruption signal needs to be greater than the noise to be detected. For example, if a volcano is obscured from satellite view due to clouds (noise), the ash plume (signal) would need to break through the clouds to be detected. This applies to the infrasonic eruption signal relative to ocean and wind noise or lightning generated by processes in the ash plume relative to lightning from a local thunderstorm. Similar to eruption onset, the eruption does not necessarily end when we no longer detect it. Additionally, in many cases data latency (satellite, infrasound) also contributes to discrepancies between eruption start and detection time.

In this study we retrospectively characterize the 2019 VEI 4 eruption of Ulawun Volcano, Papua New Guinea, on 24–26 June to evaluate the state-of-the-art in remote observational tools for an open system eruption. Analyses of data from infrasound, lightning, and satellite-borne sensors, combined with plume modeling based on these observations, indicate that the eruption started ~38 h prior to the Plinian phase with ~13 h of gas jetting captured by a regional infrasound array and corroborated by a TROPOMI SO_2 observation five times greater than background emissions. In a companion paper (McKee et al., 2021), we conducted a similar analysis of a recent VEI 4 at a closed system volcano (Raikoke, Kuril Islands). Together, these two studies demonstrate that, while remote observations are sufficient for detection and tracking *syn*-eruptive changes, key challenges in data latency, acquisition, and synthesis, must be addressed to improve near-real-time characterization of eruptions at minimally or unmonitored volcanoes.

A goal of the Earth science community is to enhance and cultivate infrastructure around archiving data for its reuse under the FAIR data principles (National Academies of Sciences, Engineering and Medicine, 2020; Stall et al., 2018; Wilkinson et al., 2016). FAIR data are Findable, Accessible, Interoperable, and Reusable. Volcanology is a multidisciplinary field that relies on a myriad of data types. Given the community's goal, we note in the Data and Discussion sections the FAIR classification of the data we used.

2. Ulawun volcano

Ulawun (5.05°S, 151.33°E, 2334 m), a Decade Volcano (UN, 1987) located on the island of New Britain in the Bismark volcanic arc, Papua New Guinea, results from northward subduction of the Solomon Sea microplate beneath the Bismark microplate at rates of over 20 cm/year (Fig. 1a); (Silver et al., 2009; Wallace et al., 2004). Ulawun has a symmetrical and heavily vegetated stratovolcanic edifice with a central vent located inside an older caldera structure (Fig. 1b). Its earliest dated eruption occurred on March 11, 1700. It then experienced 11 minor (VEI 1–3) eruptions before a major (VEI 3) eruption in January–February 1970 prompted evacuation of local residents and produced lava flows and pyroclastic density currents (reported as nuées ardentes) (CSLP, 1970). Six minor (VEI 1–3) eruptions occurred between 1973 and 1984 (GVP, 2013). Increasing unrest prompted an evacuation of 700 residents before the (VEI 3) November 17–22, 1985 eruption, which consisted of Strombolian activity with ejections of incandescent lava fragments to heights of 300–500 m above the crater, lava fountaining at the summit, and a lava flow that extended 5.5 km from the crater (Global Volcanism Program, 1983). Four minor (VEI 1–2) eruptions occurred between 1989 and 1999 (GVP, 2013), and largely consisted of small discrete ash emissions. A major (VEI 4) eruption that began on September 28, 2000 prompted evacuation of nearly 4000 local residents (GVP, 2000). This short-lived eruption produced ash plumes to 15 km, heavy ashfall, and three pyroclastic density currents, but no lava flow. After a few months of relatively low surface activity, a VEI 3 eruption on April 25–30, 2001, occurred from the main vent with minor activity from the northern flank vent and produced plumes to 14 km, triggering localized evacuations. This eruption was followed by 15 very minor eruptive activities of VEI < 1 before the 2019 eruptions.

Ulawun has been monitored by a single seismometer since 1976, and for deformation using various tilt methods (dry tilt, EDM, tiltmeters) (GVP, 1978, 1989, 2000). Noted changes in seismic activity have led to several successful eruption forecasts. GVP reports that information provided by the Rabaul Volcano Observatory suggest that, between episodes of major eruption, Ulawun is a persistently restless volcano (e.g., Rodgers et al., 2013; Roman et al., 2019), characterized by sustained activity, including high or variable seismicity rates, strong degassing, and sporadic explosions. GVP reports from 1982 to 2019 indicate background levels of 100–1800 low-frequency seismic events per day and persistent steaming, as well as cycles of inflationary and deflationary tilt and minor (phreatic) explosions. Beginning in 1998, an increase in high-frequency seismicity began and persisted until the 2000 VEI 4 eruption, suggesting that new magma may have been emplaced over this time period.

3. Data and methods

We utilize primarily infrasound, lightning, and satellite remote sensing (thermal, UV, and visible) data in our analyses, but we also checked additional data types (Table 1). We do not have *syn*-eruptive MODIS thermal observations because of acquisition rate and cloudy conditions. VIIRS data were inconclusive due to cloud cover. Ulawun volcano is too heavily vegetated for InSAR techniques and the closest seismic station with openly available data is >20 km away. Here we give a brief overview of the data and methods with more details available in McKee et al. (2021) and highlight additional available data and methods.

3.1. Infrasound

Infrasound (sound at frequencies below human hearing, 20 Hz (Bedard Jr. and Georges, 2000)), generated by volcanic processes (e.g. explosions, gas jetting, lahars, pyroclastic density currents, sub-Plinian to Plinian eruptions) is a critical tool for analyzing eruption process and detection of eruptions (e.g., Fee and Matoza, 2013; Matoza et al.,

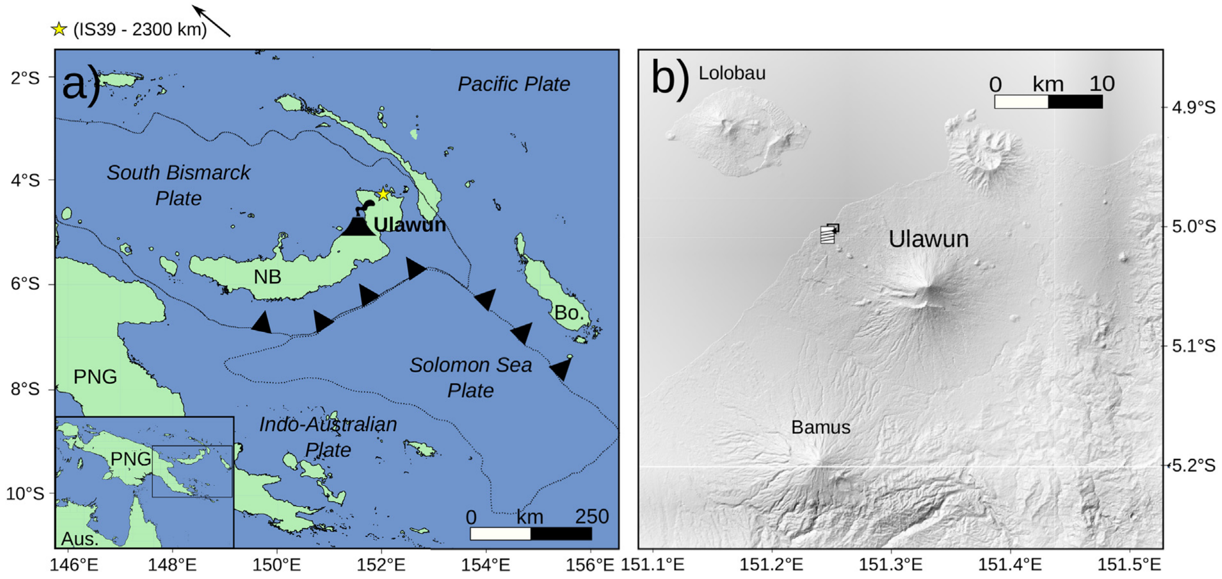

Fig. 1. Map of Volcanoes with tectonic context. a) and b) Ulawun Volcano, Papua New Guinea. Aus = Australia, PNG = Papua New Guinea, NB = New Britain, Bo = Bougainville. The two infrasound arrays nearest to Ulawun are shown in (a) with yellow stars: IS40 is ~114 km NE of Ulawun and IS39 (star directly above panel a) is 2300 km NW of Ulawun. (For interpretation of the references to color in this figure legend, the reader is referred to the web version of this article.)

2019; and references therein). Here we examine the waveform characteristics and signal frequency content of the Ulawun eruption as these provide and relate to eruption onset and duration, type of activity, and variations in eruption (e.g., Fee et al., 2017, 2013; Johnson et al., 2018; Marchetti et al., 2009; Matoza et al., 2009).

As in McKee et al. (2021), we use data from the infrasound component of the International Monitoring System (IMS). We utilize the two arrays nearest to Ulawun: IS40 (with five out of eight elements available at 114 km) and IS39 (with six out of seven elements available at 2300 km). We examined data from the IS22 array, but there were no detections likely because it is upwind for stratospheric ducting at this time of year. The infrasonic sensors sample the pressure field in the vicinity of the sensor at 20 Hz. We use the Median Cross-Correlation Maxima (MdCCM) technique (e.g., Bishop et al., 2020; Lee et al., 2013; Wilson et al., 2003) combined with a weighted least squares estimation of a plane wave arrival (Olson and Szuberla, 2008) to detect coherent infrasound and estimate the back-azimuth and apparent velocity of the incident plane wave. This information can be used to filter for signals of interest, i.e. infrasound from Ulawun. We use a window of 30 s with a 50% overlap and filter the IS40 and IS39 data from 0.5 to 5 Hz. The lower bound is 0.5 Hz to reduce the coherent acoustic noise in the microbarom frequency band and the upper bound is 5 Hz to improve the signal to noise ratio by removing higher frequency noise. Microbaroms are a ubiquitous feature in the 0.1–0.5 Hz band (den Ouden et al., 2020) and originate from standing ocean waves (e.g., Posmentier, 1967). As such, microbaroms appear as a coherent noise source in the frequency band of interest. We used the multitaper method (Riedel and Sidorenko, 1995) for power spectral density estimates on time windows with detections ±10 degrees back-azimuth to the volcanoes.

3.2. Lightning

While lightning emits radiation across a range of frequencies, we utilize the very low frequency band (VLF, 3–30 kHz) as it is detectable at up to 4000 km (Behnke and McNutt, 2014). VLF signals from volcanic lightning were detected and recorded by the Global Lightning Dataset (GLD360, operated by Vaisala Inc.).

Multiple processes generate charge within eruption columns and clouds, including fracto-emission (fragmentation of solidified magma into ash which releases charge into the plume); (James et al., 2008, 2000); triboelectrification (the transfer of charge between particles when they interact); (Forward et al., 2009; Houghton et al., 2013; Méndez Harper and Dufek, 2016; Williams et al., 2009); and at temperatures <-20°C, non-inductive ice charging (Arason et al., 2011; Prata et al., 2020; Van Eaton et al., 2020). Electrical charge is generated in volcanic plumes through ash formation and interactions, and ice-charging similar to thunderstorms (Arason et al., 2011; Forward et al., 2009; Houghton et al., 2013; James et al., 2000, 2008; Méndez Harper and Dufek, 2016; Prata et al., 2020; Van Eaton et al., 2020; Williams et al., 2009). Previous studies suggest volcanic lightning may be one of the first indicators of an explosive, ash-bearing eruption at remote volcanoes (McNutt and Williams, 2010).

For this analysis we use GLD360 globally detected lightning strokes located within 100 km of Ulawun. For each stroke the GLD360 records

Table 1
Data Accessibility and Analyses. The columns show the data types and their respective instruments or networks analyzed for each period of the eruption sequence. The rows then highlight whether the data and analyses were utilized or checked, but inconclusive.

	Pre-Eruption	Syn-Eruption	Post-Eruption
Utilized	Thermal (**MODIS, ASTER**) and Passive SO2 (**OMI, Sentinel-5P/TROPOMI**) time-series; Satellite Imagery (**Sentinel-2**, PlanetLabs); GVP Reports summarizing seismicity/tilt levels	Satellite Detections: Ash (Himawari), SO2 (**OMI, Sentinel-5P/TROPOMI**); Lightning (GLD360); Infrasound (IMS data); Plume Heights	Satellite Detections: SO2 (**OMI, Sentinel-5P/TROPOMI**); Deposition Identification: Thermal (**ASTER, Sentinel-2**) and Visible (**Sentinel-2**); Topography Change (**Sentinel-2**, PlanetLabs)
Inconclusive (checked)	InSAR (ALOS-2); Thermal (VIIRS); Seismic at >20 Km distance (**AU RABL** in IRIS DMC)	Thermal (VIIRS); Seismic at >20 Km distance (**AU RABL**)	Thermal (VIIRS); Seismic at >20 Km distance (**AU RABL**)

Bold indicates data can be formally classified as FAIR—Findable, Accessible, Interoperable, Reusable.

the time, location, estimated peak current (kA), and polarity. There is an estimated error radius of <5 km on the location of the lightning strokes (Said and Murphy, 2016). We visually inspected the lightning data for meteorological strokes determined by the timing and location of the stroke in relation to satellite plume imagery. For this eruption we determined that all strokes recorded within 100 km of Ulawun by the GLD360 network were volcanic so no strokes were removed from the dataset. In total there were 1,522 volcanic lightning strokes included in this analysis.

3.3. Satellite remote sensing

Satellite measurements are crucial for eruption characterization when ground-based instrumentation is unavailable (Poland et al., 2020). To characterize the Ulawun eruption, we examined four primary types of satellite volcanic monitoring data: SO_2 measurements, visible, thermal IR, and ground deformation (InSAR). Table 2 shows the satellite remote sensing data products we examined and our level of post-processing in characterizing the Raikoke (McKee et al., 2021) and Ulawun eruptions with infrasound (IMS array) and lightning (GLD360) included at the bottom for comparison.

Several operational UV and IR satellite instruments can remotely monitor volcanic SO_2 emissions, including both 'passive' and pre-eruptive degassing and eruptive emissions (e.g., Carn et al., 2017, 2016). Here, we use SO_2 data from the UV Ozone Monitoring Instrument (OMI), in orbit on NASA's Aura satellite since 2004, to constrain long-term, baseline SO_2 emissions at Ulawun (Carn et al., 2017), and the TROPOspheric Monitoring Instrument (TROPOMI), launched in October 2017 on the European Space Agency (ESA) Sentinel-5 Precursor (S5P) satellite (Theys et al., 2017), to analyze SO_2 emissions from Ulawun in 2019. TROPOMI SO_2 data products are available from May 2018 onwards.

Visible and thermal remote sensing can provide information about the reflected and emitted energy from the surface of the earth. Visible Near Infrared (VNIR) and Short Wave Infrared (SWIR) sensors primarily detect reflectance and have smaller pixel sizes to their thermal counterparts, are available on a number of instruments (e.g., ASTER, Landsat, Sentinel-2) and are effective at identifying healthy vegetation (e.g., Carlson and Ripley, 1997). We use these advantages to identify changes in the shape and size of volcanic edifices, the emplacement location of volcanic deposits, and any effects the eruption may have had on the surrounding vegetation. SWIR data can also be useful in detecting particularly hot volcanic features (e.g., Massimetti et al. (2020)), however the SWIR images surrounding the eruption that may contain these features were obscured by clouds. Surface temperatures can be derived from Thermal Infrared (TIR) data. By examining how surface temperature changes over time, it is possible to identify pre-eruptive changes in thermal output caused by a changes in the system, co-eruptive changes corresponding to the location of active flows, and post-eruptive changes (e.g surface temperatures remaining high or decreasing) that could help to identify the likelihood of a subsequent eruption in the near future.

We use Himawari-8 thermal data and atmospheric temperature profiles to estimate maximum plume heights. This was done by using band 13 to determine the brightness temperature of the ash plume at a wavelength of 11 μm (Prata and Grant, 2001). If the centre of the identified ash plume was colder than the surrounding ash, the coldest BT11 was selected from this region. The atmospheric temperature profile, sourced from the European Centre for Medium-Range Weather Forecasts *Re*-analysis-Interim (ERA-Interim)(Berrisford et al., 2011; Dee et al., 2011), was then used to interpolate at which height the coldest BT11 temperature, i.e., the highest height of the plume, corresponds to in the atmosphere. In contrast, if the centre of the identified ash plume was hotter than the surrounding ash, we assumed that the plume reached the stratosphere. As a result, the hottest pixel from this central region was selected and the stratospheric atmospheric temperature profile was used to calculate the maximum plume height. The uncertainty on these measurements was calculated as +/− 2 k on the BT11 (Prata and Grant, 2001), which we will call the maximum and minimum plume heights. This procedure was done to calculate plume heights for each Himawari-8 satellite image where the volcanic ash plume was seen to determine a maximum plume height time series. All this analysis was done using MATLAB.

Sentinel-2 VNIR and SWIR data were used to examine spatial changes in healthy vegetation, and TROPOMI/OMI SO_2 data to gain insight into eruption intensity and magnitude, and to identify potential eruption precursors manifested in SO_2 emissions. Carn et al. (2017) reported annual mean SO_2 fluxes for all volcanoes with emissions detected by OMI since 2005. For Ulawun, the mean SO_2 emission rate in 2005–2015 was ~630 ± 580 tons/day, which provides valuable context for interpretation of short-term SO_2 degassing rates. We used the offline Level 2 TROPOMI SO_2 data product (S5P_OFFL_L2__SO2, version 1.01.07) to investigate SO_2 degassing on shorter timescales prior to and during the 2019 eruption. Although the eruption generated a stratospheric SO_2 cloud that persisted in the atmosphere for some time, a detailed analysis of the long-range transport and lifetime of the volcanic cloud is not covered here.

3.3.1. ASTER

The ASTER sensor was launched on the Terra satellite, and compared to MODIS, has a much higher spatial resolution (90 m pixels) but a lower temporal resolution (16 day repeat time at the equator) (Yamaguchi et al., 1998). The increased spatial resolution of these data enables ASTER to detect lower temperature and/or smaller thermal features. ASTER's ground surface temperature (AST_08) data product was used to develop a time series of the thermal flux above background (similar to Reath et al., 2019b) before the Ulawun eruption. These data were unavailable during the eruption due to cloudy conditions and a lack of data acquisitions. ASTER data are openly available at several locations online including NASA Earthdata Search (https://search.earthdata.nasa.gov/search) and the U.S. Geological Survey (USGS) EarthExplorer (https://earthexplorer.usgs.gov/).

3.4. Plume modeling

Integral plume models, based on buoyant plume theory (Morton et al., 1956), are used to investigate the source conditions and the dynamics of sustained volcanic plumes by assuming the eruption column is in steady-state and the rate of entrainment of ambient gases into the plume are proportional to the plume velocity. Despite their simplicity, integral plume models can account for additional volcanic processes such as wind, humidity, phase changes and particle fallout (Bursik, 2001; Glaze et al., 1997; Mastin, 2007; Woods, 1993). These models have become part of operational forecasting to better monitor explosive eruption and subsequent tephra dispersal (Scollo et al., 2012).

We determine an initial Mass Eruption Rate (MER) time series of the Ulawun eruption by using the integral buoyant plume model of Degruyter and Bonadonna, 2012. This is done in the same manner as in McKee et al., 2021. As the initial conditions of the eruption column are unknown, we apply a Monte-Carlo approach that is constrained with the minimum and maximum observed plume heights (see Section 3.3). The parameter space used in the Monte-Carlo modeling can be found in Sup. Table 1. If the maximum plume height is unavailable, the average plume height is used as the upper constraint. To account for the effect of wind when modeling the volcanic plume, the integral buoyant plume model is run first without wind and then with wind. This is because in some cases the addition of the radius to the top centerline height of a modelled plume that considers wind can go higher than the same case where wind is not considered. As a result, we take a similar approach to Mastin, 2014 and choose the minimum top modelled plume height from the case with no wind and the case with wind, where the top plume height is defined as the top centerline

Table 2
Data products, post-processing, and characteristics.

Instrument	Product	Level of Post-processing	Spatial Resolution	Time Resolution	Sensitive to/Measures	Other info	Reference(s)
ALOS-2	Level 1.1, Ultra fine	coregistration, georeferencing, interferogram generation, atmospheric, topographic, and flat earth corrections, and phase unwrapping	3 m	14 day repeat time	Radar reflectivity	L band	https://www.eorc.jaxa.jp/ALOS/a/en/alos-2/a2_about_e.htm
ASTER[*]	Level 2 Surface Kinetic Temperature	Back ground temperature correction, thermal feature identification	90 m	16 day repeat time	Land surface temperature	bands 10 through 13	Reath et al., 2019b
Himawari	visible and IR satellite images	conversion of band 13 IR values to degrees C	0.5 km for band 3; 2 km for band 13	10 min (2.5 min in rapid scan mode)	visible and IR	bands 3 and 13	https://www.data.jma.go.jp/mscweb/en/himawari89/space_segment/spsg_ahi.html
MODIS	Level 1B Calibrated Radiances	Conversion of radiances to brightness temperature, then selection of pixel of interest	1 km	4 per day	IR		https://ladsweb.modaps.eosdis.nasa.gov/search/order/1
OMI	Level 2 SO2 columns	Mapping and conversion to SO2 mass	13 × 24 km at nadir	1 per day	SO2, volcanic ash		(Carn et al., 2017, 2013)
PlanetScope[*]	4-band PlanetScope scene	None	3 m (resampled)	Variable; >2 per day possible	visible, NIR		Planet Team, 2017
RADARSAT-2[**]	Wide ultra-fine	Amplitude image	3 m	24 day repeat time	Radar reflectivity	C-band at 5.405 GHz	https://earth.esa.int/web/eoportal/satellite-missions/r/radarsat-2
Sentinel-2	Falsa Color and NDVI	None	10 m	10 day repeat time	visible, vegetation		https://www.sentinel-hub.com/explore/eobrowser/
TROPOMI	Level 2 SO2 columns	Mapping and conversion to SO2 mass	3.5 × 5.6 km at nadir	1 per day	SO2, volcanic ash		Theys et al., 2017
VIIRS	IR satellite images	None	750 m	2 per day	IR		(Cao et al., 2014, 2013)
IMS infrasound arrays	Waveforms, array processing detection lists	Array processing (possible real-time)	1902 km average station spacing for complete IMS network	20 samples/s.	acoustic pressure wave [Pa]	High or Low elements	(Christie and Campus, 2010)
GLD360	Lightning strokes: location, polarity, estimated peak current	None	global coverage, sensor locations not disclosed	100 k Samples/s	VLF Time of Arrival and Magnetic Direction Finding		Said et al., 2010

[*] Ulawun only;
[**] Raikoke only.

plus the radius in the latter. For each run in the Monte-Carlo simulation (2000 runs), if the top modelled height lies between the minimum and maximum calculated observed plume heights, the initial modelled MER is recorded. An average is taken of all that ‘matched’ initial modelled MER. The minimum and maximum ‘matched’ MERs are also recorded. This is repeated for each time that an observed plume height was calculated. Meteorological data from during the eruptions is sourced from ERA-Interim.

4. Results and observations

4.1. Infrasound

We detect the Ulawun eruption with IMS arrays IS40 and IS39 (Supplementary Figs. S1, S2). We observe two eruptive episodes with the IS40 array and only the second of those episodes with the IS39 array. In Fig. 2a, we show the best beam of the IS40 array data, and the colored dots indicate detections from Ulawun. We detect about 13 h of near-continuous emissions from Ulawun on 24 June 2019 from 10:39 to 23:18 UTC and another 11 h of continuous emissions from 25 June at 19:28 to 26 June at 6:44 UTC. The first episode is lower amplitude than the second, the peak frequency increases slightly over the 13 h, and there may be harmonics (Fig. 2a, b). In Fig. 2b, we highlight the peak frequency through time over the full spectrogram using unfiltered data. In the second episode, the peak frequency increases over several hours from ~0.3 Hz to ~0.6 Hz and then it decreases over the remainder of the eruption to ~0.09 Hz. We also observe this overall decrease in the peak frequency in comparing the spectral curves of different eruptive periods. Fig. 2c shows these spectral curves, where the color of the curve matches the detections in Fig. 2a. The decrease in infrasound peak frequency in the second episode coincides with the increase in eruptive intensity documented by a local helicopter pilot (Fig. 2 panels 1–5).

4.2. Lightning

We determined the initial lightning stroke to be on 26 June at 01:21:56.408 UTC (Fig. 3). Lightning continued for over 6 h until the final stroke at 08:04:12.408 UTC (Fig. 4a). We observed peak stroke rates from 06:00 to 08:04 UTC reaching 25 strokes per five minutes (Fig. 4a). The peak current measured for a single stroke during this eruption was +130.5 kA (Fig. 4b). The majority of the strokes were in-cloud, with a mix of positive and negative polarities. The first pulse has fewer strokes and they are located to the east of Ulawun (Fig. 3), while the second and third pulses have more strokes and are located over Ulawun. Lightning stroke rates show a clear ramp up-peak-ramp down in each pulse (Fig. 4a).

4.3. Satellite remote sensing

Several different sensors observing the VNIR, SWIR, and TIR wavelengths provided valuable information for the study. In an attempt to identify pre-eruptive unrest, we analyzed high spatial resolution (i.e., ASTER) TIR data before the eruption and were unsuccessful due to cloudy weather conditions and a lack of regular acquisitions. The most recent cloud-free observation was made on 21 May 2019, approximately two months before the eruption. Although a volcanic thermal

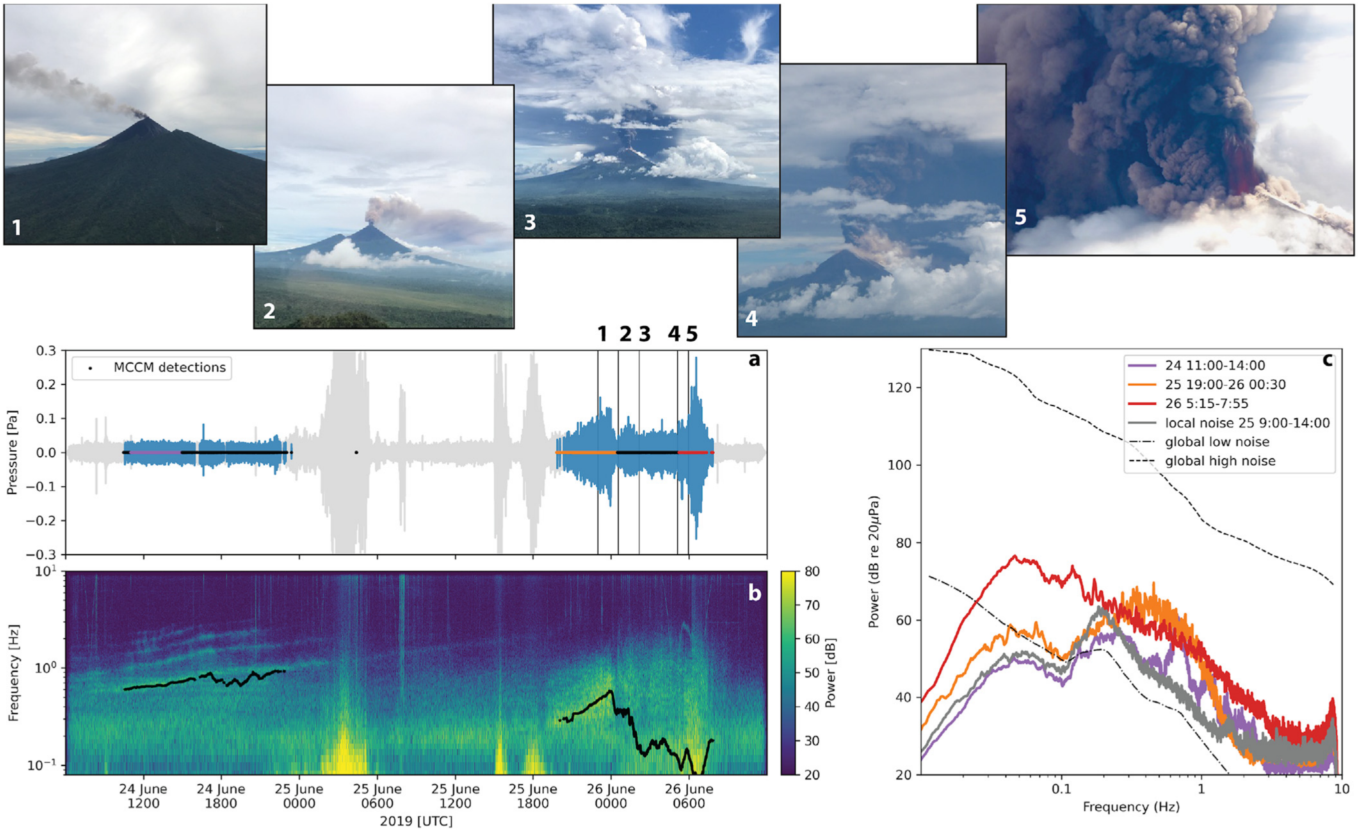

Fig. 2. Ulawun Eruption Infrasound analysis. a) Beamformed waveform from IS40 array with MdCCM detections plotted as black, red, and green dots, b) Spectrogram with the peak frequency through time highlighted by the black line, c) Spectral curves for specific window of the eruption. The color of the spectral curve corresponds to the color of MdCCM detections in a. The gray curve is the noise from 25 June 09:00–14:00. The dashed curves are the International Data Centre (IDC) infrasound global low and high noise models for IMS infrasound arrays (Brown et al., 2014). Photos 1–5 courtesy of Craig Powell. (For interpretation of the references to color in this figure legend, the reader is referred to the web version of this article.)

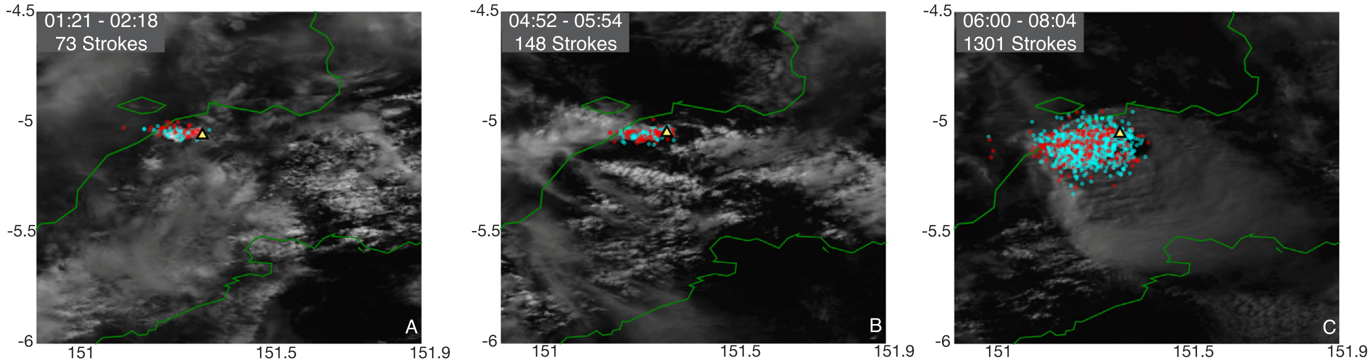

Fig. 3. Ulawun eruption satellite observations overlain with lightning locations. Visible light satellite images from Himawari, Red is positive, blue is negative, the yellow triangle shows the volcano location, and green outlines are the landmass. (For interpretation of the references to color in this figure legend, the reader is referred to the web version of this article.)

feature was observed at this time, it was within background levels of thermal output at Ulawun over the past decade.

We determined the eruption column height from Himawari data for the Ulawun eruption (Fig. 3). We first identified the developing plume from the eruption at 02:00 as puffs from the vent (Fig. 4c). A stronger pulse starts at 04:50 UTC and peaks at 06:20 UTC, where a plume height of 26.1 km asl is observed. The pixels located in the center of the umbrella cloud are hotter than the pixels surrounding them. This is evidence that the central plume reached the stratosphere and started to heat to the ambient temperature.

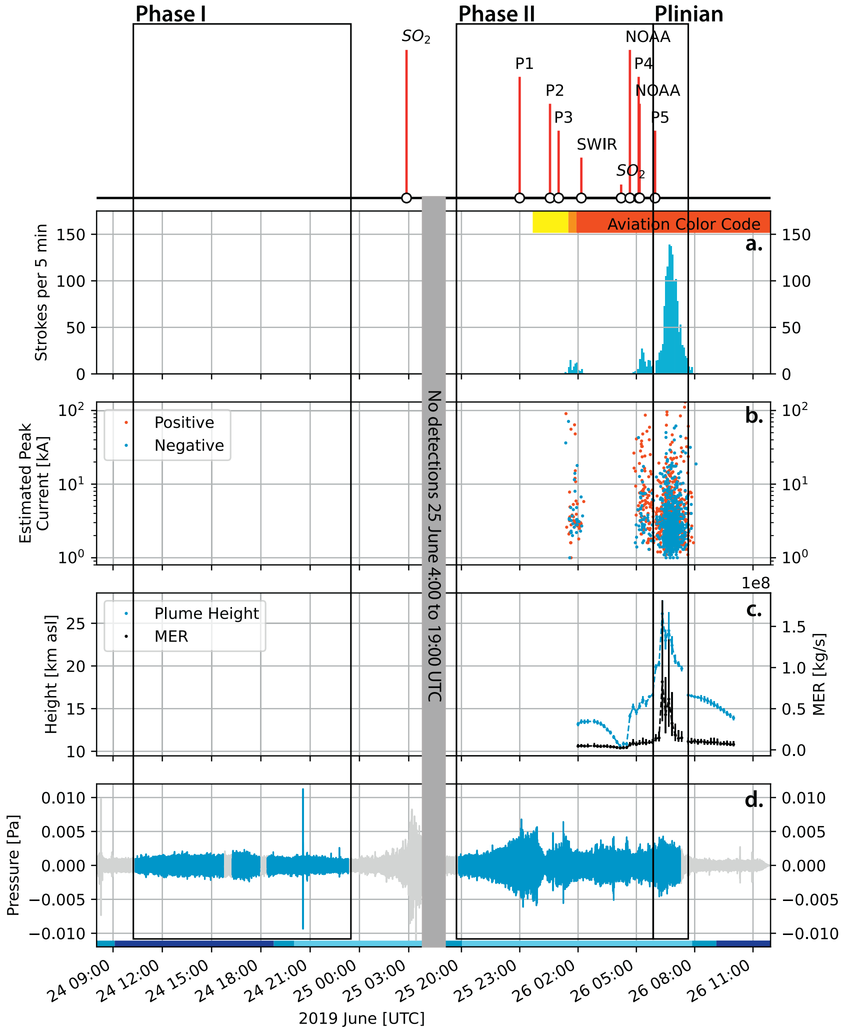

Fig. 4. Comparison of lightning, plume height, mass eruption rate (MER) and infrasound at Ulawun. a) Lightning strokes per 5 min, b) Estimated peak current per stroke (red is positive; blue is negative), c) Plume height (10 min increment) in blue and MER in black estimated from plume height with vertical lines showing the error, d) Beamformed infrasound trace with times of coherent detections plotted in blue. Infrasound data are filtered from 0.1 to 5 Hz. (For interpretation of the references to color in this figure legend, the reader is referred to the web version of this article.)

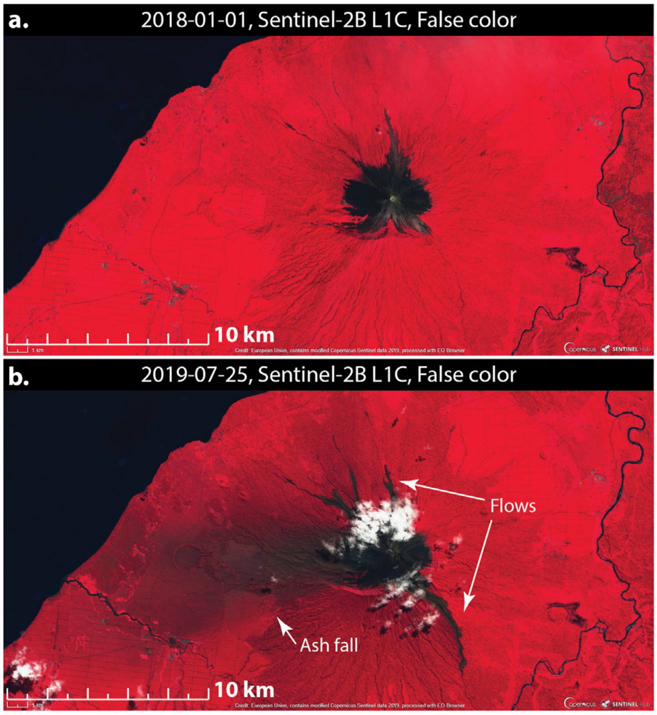

Fig. 5. Post-Eruption Ulawun - Thermal observation of lava/lahar and ash fall from Sentinel-2 VNIR images from a) January 1, 2018 and b) July 25, 2019.

ASTER TIR observations made on 29 June 2019 revealed the location of still-cooling flows (Supplementary Fig. S6) and Sentinel-2 VNIR observations made on 25 July 2019 revealed the extent of terrestrial ash coverage made during the first eruptive pulse (Fig. 5). Further, we compared Sentinel-2 acquisitions made before and after the eruption to reveal the *syn*-eruptive expansion of the crater (Supplementary Fig. S7); these findings were confirmed by PlanetScope visible imagery (Fig. 6; Planet Team, 2017).

As noted above, Ulawun has been a persistent source of SO_2 emissions since at least 2005, based on UV satellite observations (Carn et al., 2017). Nevertheless, based on inspection of daily UV satellite SO_2 data (https://so2.gsfc.nasa.gov/), no significant SO_2 emissions from Ulawun were apparent for ~8 months prior to the June 2019 eruption; the last, clear detection of SO_2 by OMI was in mid-October 2018, consistent with GVP reports of minimal activity at the volcano from late 2018 to June 2019. TROPOMI detected a weak SO_2 plume (~100 tons SO_2) on June 24; this emission was not anomalous relative to decadal average SO_2 emissions from Ulawun, but it was the first clear SO_2 detection at the volcano for several months. Much stronger SO_2 emissions were observed on June 25 at ~02:50 UTC (Fig. 7). Using wind data from the NASA Goddard Earth Observing System, version 5 (GEOS-5) atmospheric model coupled with the TROPOMI SO_2 columns (Fig. 7), we estimate an SO_2 flux of ~3100–3600 tons/day from Ulawun on June 25 using a 'plume traverse' method (Theys et al., 2017), which is significantly above the long-term mean emission rate (~630 tons/day). Further strong SO_2 degassing was observed by TROPOMI on June 26 at ~04:10 UTC (total SO_2 mass of ~5–7 kt depending on plume altitude; Fig. 7), ~2 h before the Plinian phase of the eruption at ~06:00 UTC (based on lightning stroke rates).

Following the Plinian phase of the Ulawun eruption, from June 27 TROPOMI and other UV satellite instruments detected a stratospheric cloud containing ~0.15 Tg SO_2 that persisted in the atmosphere for at least 2 weeks (Fig. 8). In terms of SO_2 release, this was the largest eruption of Ulawun measured since October 1980 (~0.2 Tg SO_2; Carn et al., 2016). However, another major eruption occurred at Ulawun just over a month later on August 3, 2019 and the combined total SO_2 emission for the June and August 2019 eruptions (~0.34 Tg) is the largest on record for this volcano.

4.4. Plume modeling

We used buoyant plume modeling to estimate the MER for the Ulawun eruption. Fig. 4c shows the MER results for the Ulawun eruption. From the maximum height, we calculated a MER that ranged between 3.29×10^7 and 1.82×10^8 kg/s and has an average value of 8.27×10^7 kg/s. Based on these time series, we have also estimated a total erupted mass (TEM) of 3.34×10^{11} kg (maximum estimate of 5.87×10^{11} kg and minimum estimate of 2.01×10^{11} kg).

4.5. Local observations

Rabaul Volcano Observatory (RVO) reported occasional good visibility of the summit until dusk on 24 June local time (23 June 14:00 to 24 June 14:00 UTC). They observed a weak and thin white vapor plume with no visible glow or audible noise. On 25 June local time (24 June 14:00 to 25 June 14:00 UTC) they also reported occasional good visibility of the summit until dusk. They observed small to moderate volumes of thick gray ash clouds that rose about 100 m above the summit crater and drifted to the southeast until mid-morning. At around 8:00 pm local time (25 June 10:00 UTC) they observed a weak glow on the eastern side of the volcano and heard two weak rumbling noises originating from the eastern side.

5. Discussion

5.1. Timeline and characterization of the 2019 Ulawun eruption

Our observations indicate that the Ulawun eruption comprised three distinct phases: Phase I, Phase II, and a Plinian phase (Fig. 4). Phase I

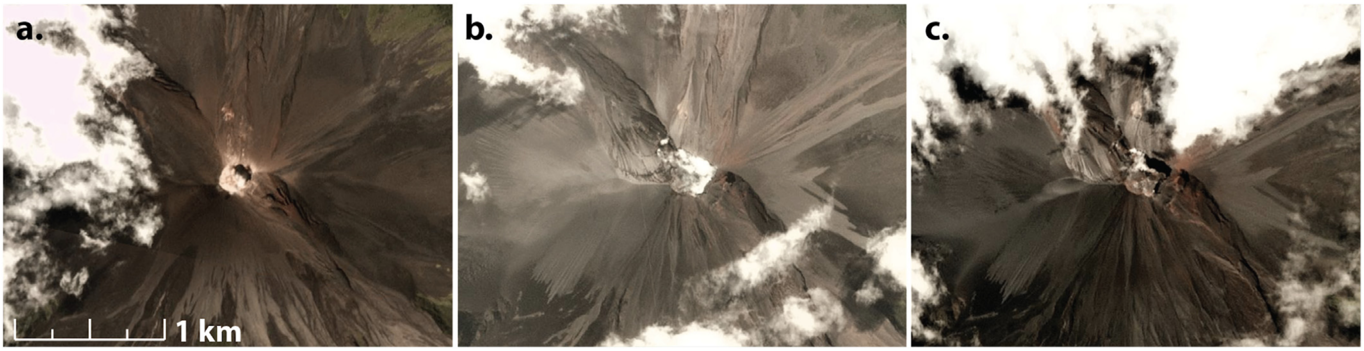

Fig. 6. Change in crater morphology at Ulawun from PlanetScope imaging (Planet Team, 2017). Images show Ulawun on (a) May 25, 2019 at 23:52 UTC (May 26, 09:52 local time); (b) June 26, 2019 at 23:37 UTC (June 27, 09:37 local time; crater partly obscured by degassing); and (c) July 17, 2019 at 23:54 UTC (July 18, 09:54 local time). Crater area measured on May 25, 2019 was ~35,000 m^2; on July 17 the crater area was ~66,000 m^2.

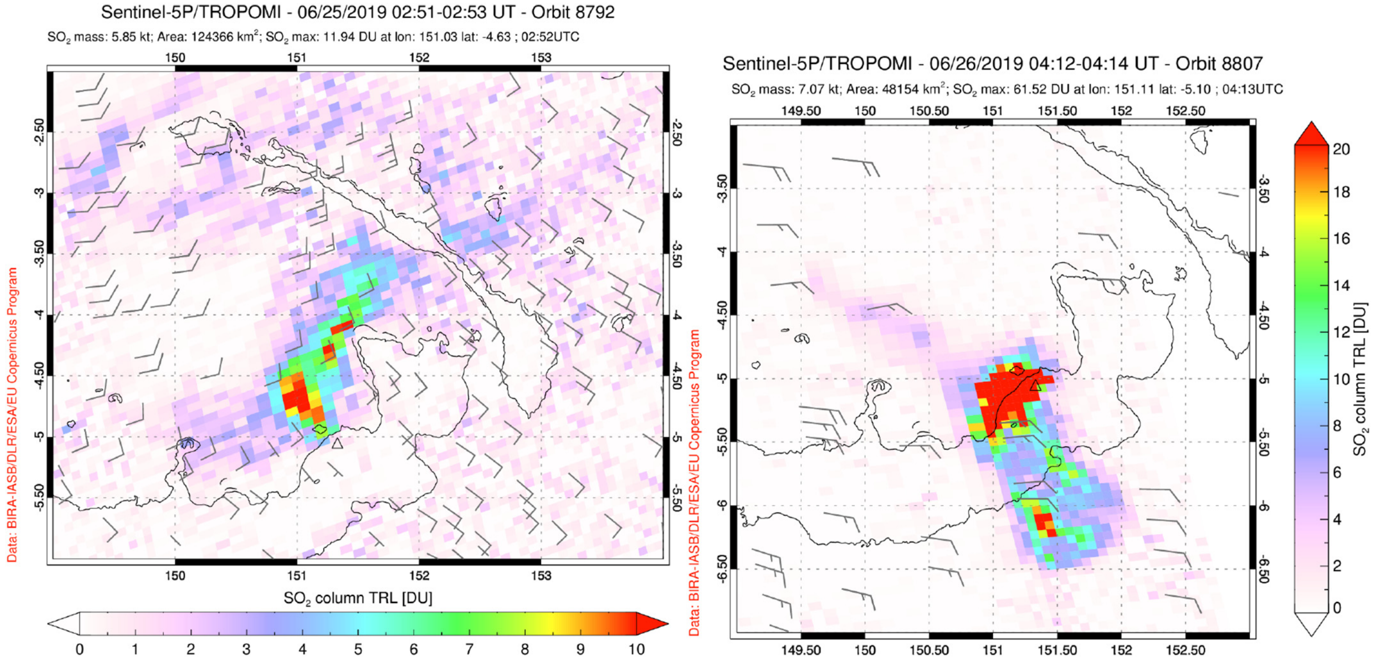

Fig. 7. Sentinel-5P/TROPOMI SO_2 data for Ulawun on June 25–26, 2019. Wind barbs show coincident NASA GEOS-5 model wind direction and speed at the altitude of Ulawun (small tick = 5 knots; large tick = 10 knots). June 25: first significant increase of SO_2 degassing (estimated SO_2 flux is ~3100–3600 tons/day, significantly above the long-term average at Ulawun); June 26 (~04:00 UT, just prior to Plinian phase): continued elevated SO_2 degassing, plume dispersal decoupled from wind direction at vent altitude, indicating stronger emissions.

began after nightfall on 24 June at 10:39 to 23:18 UTC and was mainly observed with infrasound, but is shortly followed by an SO_2 observation on 25 June at 2:51 UTC with an estimated SO_2 flux of ~3100–3600 tons/day, well above the decade-long average for Ulawun of 630 tons/day (Carn et al., 2017). We do not observe an ash plume during this period, however observations were limited due to time of day (i.e. after nightfall). This suggests that Phase I involved pure gas jetting. Phase II started on 25 June at 19:28 UTC when infrasound detections began again with several hours of gas jetting. RVO's observations suggest activity started sooner, but was not detected remotely. The infrasound signal continued and the first ash plume detection followed at 00:30 UTC. Lightning was first detected on 26 June at 01:21:56.408 UTC. In Phase II there were two pulses of lightning and ash plume detections with a pause in between them while the infrasound remains continuous. SO_2 emissions were above background during this phase as observed during a TROPOMI overpass on 26 June at 4:12 UTC. The pilot photos show an increase in the presence of ash over the course of Phase II (Figs. 1–3), which coincides with the onset of lightning and ash plume detections. The Plinian phase began on 26 June at ~06:00 UTC. At approximately this time, the plume height and lightning stroke

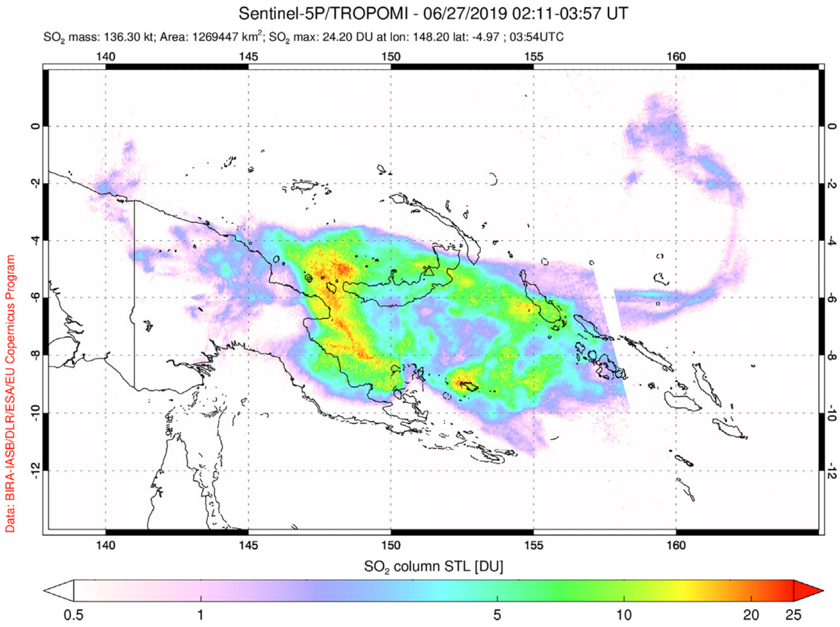

Fig. 8. Sentinel-5P/TROPOMI SO_2 data for Papua New Guinea on June 27 showing the upper tropospheric and stratospheric SO_2 cloud produced by the June 26 Plinian eruption of Ulawun (~0.14 Tg SO_2).

rate increased, the infrasound frequency dropped and the pilot photos document a lava fountain. The Plinian eruption column produced a strong umbrella cloud that reached the stratosphere, with the lightning strokes centered in this cloud (Fig. 3b), suggesting little to no wind shearing. The lightning and ash plume detections temporally align, showing three pulses, while the infrasound was continuous through Phase II and the Plinian phase. The infrasound detections end on 26 June at ~06:44 UTC followed by the last lightning stroke at 08:04 UTC and ash plume detection at 10:00 UTC. SO_2 was measurable in the atmosphere for at least two weeks. The ash plume drifted to the SW and was observable for approximately 6 h after the eruption in band 13.

5.1.1. Unrest

Ulawun volcano showed no signs of unrest that were detectable with remote observations. We did not detect deformation, but Ulawun's highly vegetated edifice limits the utility of InSAR (Ebmeier et al., 2013). We detect increased outgassing (an SO_2 anomaly) during Phase I of the eruptive sequence and discuss this further in Section 5.1.2. Ulawun is an open system with regularly observed thermal anomalies (Supplementary Fig. S5) (Wright et al., 2004), and none of the thermal anomalies detected in our study were above background for Ulawun (Supplementary Fig. S5). We do not detect unrest prior to eruption for a number of possible reasons: low InSAR coherence, satellite repeat times, thermal anomalies within background, no unrest above detection limits, and/or no precursory unrest occurred.

5.1.2. Eruption onset

Using the solid material definition, the latest possible eruption onset time for Ulawun is during Phase II on 26 June between 01:30 and 02:00 UTC as indicated by lightning, Himawari ash plume detections, and pilot photos. However, infrasound detections started in Phase I about 38 h prior to ash detections. Phase I of the eruption sequence has approximately 13 h of infrasound detections characterized as jet noise followed by an SO_2 detection with about five times the average flux for the previous decade of observations (Carn et al., 2017). Sound is produced by "any change of stress or pressure producing a local change in density or a local displacement from equilibrium in an elastic medium" (Acoustics, 2002). Therefore a volcanic process generates infrasound by accelerating the volume of air above the crater. Thirteen hours of accelerating air above the crater detected at about 120 km and followed by an almost 2 kt SO_2 detection is an highly energetic/explosive process. We note the infrasound observations at IS40 provide vastly more information than IS39 because it is closer to the source and likely more sensitive to lower level activity. Most of this phase occurred at night and was obscured from view. There may have been ash that was below our detection limits. We suggest that the infrasound detection may represent the beginning of the eruption. Alternatively, the Ulawun eruption may have been preceded by an explosive, likely pure gas emission phase. The latter possibility prompts the questions: what changed in the system? Are there other open-system Plinian eruptions that started with an explosive gas phase? What does this tell us about what happened in the subsurface? How do open systems produce Plinian eruptions?

5.1.3. Syn-eruption

We combined infrasound, lightning, satellite remote sensing and photographs to characterize the changes during the eruptive sequence. The high temporal resolution of the Himawari TIR dataset facilitated the comparison between ash plume heights and the lightning and infrasound detections. This was especially critical as ASTER missed the eruption due to the 16-day satellite repeat time. The infrasound observations well-document the eruption evolution, with an infrasonic frequency decrease capturing a change in eruption character. We have robust detections of SO_2, however the flux estimates are minimums as ash limits TROPOMI detections. The timing of the Sentinel-5P overpass was fortuitous relative to the infrasound detections as it confirmed the first phase of the Ulawun eruptive sequence.

There is a clear increase and decrease in the stroke rate as the eruption starts, strengthens, and then stops (as indicated by infrasound, plume height, and MER), which we also observed at Raikoke. The clear increase-peak-decease of lightning stroke rates for each plume may be indicative of ice-graupel charging. Initial lightning would be from ash interactions, but as each of the plumes reached 7.5 km and cooled to atmospheric temperature, (−20 °C in the ERA-Interim temperature profile for both of these volcanoes) ice-graupel charging may result in an increase in lightning strokes. This is especially likely for the longer duration Plinian phases, as we can see that again the peak lightning stroke rate coincides with the maximum eruption cloud heights (which are above the −20 °C isotherm). The lightning stays centered above the vent and, because the umbrella cloud maintains its circular shape, we do not see the same extension of lightning downwind during the Plinian phase as at Raikoke. This makes it more difficult to ascertain how much of an effect ice vs. ash charging is having on the lightning generation because we cannot assume the majority of ash has fallen out of the plume that close to the vent. Overall, it can be determined that the rates of volcanic lightning correlate with increases in plume height and MER as seen previously at eruptions such as Anak Krakatau (Prata et al., 2020) and Kelud (Hargie et al., 2019).

5.1.4. Eruption cessation

At present, the volcanology community has not reached a consensus definition for what constitutes the end of an eruption (Phillipson et al., 2013), but this is an active area of research. Manley et al. (2020) note that definitions generally fall into two categories: 1) generic rules or 2) volcano specific. For this discussion, we use a volcano-specific definition and define the end of eruption as a return to background activity, where background activity is relative to what can be detected using infrasound, lightning, and satellite remote sensing. The eruption fell below detection limits for infrasound, lightning, and ash plume detections on 26 June at about 07:10 UTC. This is the earliest eruption cessation time as there may have been continuing activity below detection limits. From a remote observational stance, background activity at Ulawun is no infrasound, lightning, deformation, but regular outgassing (Carn et al., 2017) and low-temperature thermal detections. Ulawun had two subsequent eruptions in August and September 2019 and returned to background activity in October 2019 (GVP, 2019).

5.1.5. Post-eruption

Analysis of post-eruption imagery is a powerful tool for understanding eruption dynamics and impacts and for preparing for future eruptions. We document the change in crater area as well as the ashfall deposit and cooling flow. Capturing the change in crater area required favorable weather conditions (i.e., clear skies) during satellite overpasses. In the first post-eruption image of Ulawun, the crater is obscured by the gas plume (Fig. 6). Documenting these post-eruption features required multiple satellites/instruments (e.g., Sentinel-2, ASTER, PlanetLabs), timely overpasses, and favorable weather conditions as well as higher resolutions not previously available as of 5–20 years ago.

5.2. Assessing state-of-the-art in remote eruption characterization

In eruption characterization we aim to assemble a comprehensive timeline of observations through the full eruption cycle and use it as a basis for understanding processes in a volcanic system. In this study (Part II) and the companion study (Part I, McKee et al., 2021), we characterized two eruptions with a wide range of largely-independent remote observations, as these provided the only available data, but also as a means to critically assess the state-of-the-art of remote observation technologies in application to ongoing eruptions. Here we briefly summarize the results of Part I and discuss what can and cannot be resolved through remote observation with respect to precursory unrest, eruption

Table 3
Comparison of Raikoke and Ulawun Eruption characteristics.

	Raikoke	Ulawun
Dates	21–22 June 2019	24–26 June 2019
Latitude*	48.292°N	5.05°S
VEI**	4	4
System type	closed	open
Population within 30 km*	0	10,577
First detected with	Lightning & Himawari-8	Infrasound & SO_2
Duration (time from first to last detection)		
Infrasound [hours]	12.24	44.08
Lightning [hours]	16.09	6.70
Himawari - visible eruption cloud [hours]	15.83	7.33
Max plume height (km a.s.l)	11	26.1
Max MER (kg/s)	1.62E+06	8.27E+07
Total eruptive mass*** (kg)	4.39E+10	3.34E+11
Total SO_2 mass (Tg)	1.4	0.15
Eruption Magnitude = log10(TEM) - 7	3.6	4.5
Eruption Intensity = log10(MER) + 3	9.2	10.9

* As listed on the Global Volcanism Program website for Raikoke (https://volcano.si.edu/volcano.cfm?vn=2902500) and Ulawun (https://volcano.si.edu/volcano.cfm?vn=252120).
** 2019 Raikoke eruption now listed as VEI 3 in GVP.
*** of the average values.

onset, *syn*-eruptive activity, eruption cessation, and post-eruptive activity at Raikoke, a closed system prior to eruption, and Ulawun, an open system.

5.2.1. Summary of 2019 Raikoke eruption observations and limitations

In Part I, we characterized the June 2019, VEI 4 eruption of Raikoke volcano, Kuril Islands (McKee et al., 2021). Our analysis showed no signs of precursory unrest above detection limits. The eruption started with a waxing-pulsatory phase in which we observed six eruptive pulses lasting 13 to 43 min with a similar range of interpulse times (13–33 min). The main Plinian phase followed and lasted about 3.5 h with maximum plume heights reaching 11.1 km asl. This was followed by the waning phase with several more pulses with decreasing intensity, plume heights, and lightning stroke rates. These three phases are well captured by infrasound, lightning, and satellite remote sensing data. We also documented a 14% increase in island area, an increase in crater area, and an algal bloom in the waters around Raikoke likely caused by the injection of erupted material into the water.

5.2.2. Comparison of Raikoke and Ulawun eruptions

The June 2019 eruptions of Raikoke and Ulawun both had Plinian phases and are thus considered to represent VEI 4 eruptions. Table 3 shows a comparison of the eruptions. The Raikoke eruption was first detected, albeit in hindsight, with lightning and Himawari-8, while for Ulawun it was infrasound and SO_2 from TROPOMI (Table 3). This highlights the need for diverse observational technologies as they each have their strengths and weaknesses. Infrasound and SO_2 detections were critical for detecting the start of the gas-rich, ash-poor Ulawun eruption onset. Whether or not an ash-poor onset is common for open systems would require examining additional open system eruptions. The other parameters show that while both eruptions meet the criteria for VEI 4 eruptions, they have different characteristics. Raikoke's eruption was an order of magnitude smaller in estimated total eruptive mass (TEM), but an order of magnitude larger in total SO_2 mass. Ulawun's visible eruption cloud phase lasted about half the duration of Raikoke's. An eruption's VEI can be assigned using the volume of the eruption deposits or the maximum plume altitude (Newhall and Self, 1982; Pyle, 1989; Walker, 1973). The former is not feasible for remote observations, especially in cases such as Raikoke where much of the erupted material was deposited in the ocean. Pyle (2015) summarizes the categories of VEI with respect to various eruption characteristics. We have observations for two of these characteristics: eruption column height and stratospheric injection. Column height and the occurrence of stratospheric injection are both dependent on the atmospheric structure during the eruption (Schneider and Hoblitt, 2013), which are notably different for Raikoke (high latitude) and Ulawun (low latitude) (Table 3). While eruption magnitude ($log_{10}(TEM) - 7$) and intensity ($log_{10}(MER) + 3$) (Pyle, 1995; Tsuya, 1955; Hédervári, 1963; Newhall and Self, 1982; Fedotov, 1985) are more independent measures than VEI, they rely on quantitative estimates of TEM and MER, respectively, which in our case are estimated through plume modeling and again influenced by the atmospheric structure. Raikoke's total eruptive mass, MER, and maximum plume height suggest that its eruption was smaller than Ulawun's. However, the total SO_2 mass is comparable to higher magnitude/intensity eruptions such as 1980 Mt. St. Helens and 2008 Kasatochi (Carn et al., 2003; Prata et al., 2010; Pyle, 2015).

5.2.3. State-of-the-art and limitations in remote sensing for rapid characterization of volcanic activity

In examining these two eruptions, we pooled together expertise and as many observations as we could find, which illuminated modern capabilities and continued challenges in remote eruption characterization, especially if time is of the essence. By combining the various remote observational tools, we were able to track changes in eruption intensity from three perspectives (i.e. infrasound, lightning, and ash plume height); observe differences in gas and ash emission timing; and track geomorphological changes (i.e. ash fall deposits, lava/lahar/PDC deposits, and crater geometry). With a multidisciplinary approach, the volcanology community can not only detect and characterize eruptions, but start to explore fundamental science questions using remotely-acquired data. For the open-system Ulawun eruption, a key question is what caused the change from persistent gas emissions to vigorous gas jetting, followed within 24 h by a Plinian eruption?

Through these eruption characterizations we encountered issues with data latency, processing time, temporal and spatial resolution, detection limits, noise and clutter (repetitive coherent infrasound signals from other sources that are unwanted or not the target signal (Ceranna et al., 2019; Matoza et al., 2013)) in the data, and weather. Data access quickly presented a challenge and interpersonal relationships were critical in acquiring lightning, infrasound, and some satellite remote sensing data. Characterizing these eruptions with FAIR data would have limited our data to those in bold in Table 1. We note that if strictly using FAIR data, neither eruption is missed and broad characterization is possible. The additional data provide higher spatial and temporal details allowing us to constrain changes during the eruption and individual phases. Satellite and infrasound data are both limited by latency in that it requires time to transmit satellite data to earth and for sound waves to travel from source (volcano) to receiver (array). Processing data is time-intensive, especially for data types that require manual review and processing. This was especially true in determining signal from noise and clutter. For lightning, the Himawari-8 images of the plume were critical for determining the lightning strokes associated with the eruptions. Noise (e.g. wind, ocean) and clutter remain challenges in infrasound analysis, especially as volcanic eruptions often have similar frequency content to that of the ocean microbarom, which limits our detection capabilities. Detecting the eruptions with some satellite-based observations was limited by temporal and spatial resolution. MODIS detected the Raikoke eruption, but missed the Ulawun eruption because of satellite overpass times and cloudy conditions, which limits tasked acquisitions like ASTER. MODIS detections automatically task ASTER acquisitions, as such ASTER was not automatically tasked for the Ulawun eruption. Lightning and satellite observations are powerful tools for detecting and observing eruptions, but provide limited information about an eruption as they are indirect measures of activity at the volcanic vent. Unfortunately, weather (e.g., storms, cloud cover, wind) remains a limiting factor.

We did not detect clear precursory unrest for either eruption. At Raikoke, detections of thermal anomalies and gas detections were unlikely as it was a closed system prior to June 2019 (Reath et al., 2019a). However, being a closed system suggests there would be deformation potentially detected through InSAR techniques. We did not detect deformation at Raikoke for a number of potential reasons. The deformation source may have been deep thereby limiting detection due to the island size. Deformation may have occurred between the last SAR acquisition and the eruption (i.e. a short run up time) or before the SAR acquisitions we examined (i.e. recharge long before the eruption). At Ulawun, we did not detect precursory thermal or gas anomalies prior to eruption Phase I, although there was a clear increase in SO_2 emissions prior to Phase II (Fig. 7). Anomalies prior to Phase I were possibly obscured by cloudy conditions, or Ulawun may have been temporarily closed thereby not emitting gas or heat and limiting detection of unrest. InSAR-based deformation detection was limited by poor coherence due to vegetation. It is beyond the scope of this paper to determine if these two eruptions are outliers or the norm, but they both tested our capabilities in remote detection of unrest and highlighted some current limitations.

Recent advancements in satellite data processing have shown how the automation of this processing in real-time may be helpful for remote volcano monitoring. One such example is the VOLCAT system run by NOAA/CIMSS (Pavolonis et al., 2018). For the Raikoke eruption, the VOLCAT platform first recorded an ash alert derived from Himawari-8 data on 21 June 2019 at 18:10 UTC. This corresponds to the first pulse of the eruption where lightning was first detected at 17:48 UTC. Throughout the multi-pulsed eruption the VOLCAT system derived 4 ash alerts, 2 ice alerts, and 2 thermal 'hot' alerts. Although the first alert corresponded with the first pulse of activity the next alert did not occur until Pulse 7, the main Plinian phase. For the Ulawun eruption, the VOLCAT system recorded an initial thermal 'hot' alert derived from Himawari-8 data during eruption Phase II (26 June, 01:10 UTC). This was followed by 7 additional Himawari-8 and VIIRS 'hot' alerts and with one 'ash' alert recorded the day after the eruption. Oddly, there are no archived alerts triggered by the main plume event that occurred between 06:00–08:00 UTC, which resulted in the expansive umbrella cloud, infrasound detections, and 1300 lightning strokes mentioned in this paper. These examples demonstrate how even with rapidly advancing automation of satellite techniques the combination of remote data (i.e. satellite, infrasound, lightning) combined with an expert eye is necessary to fully parse out an eruption sequence from the available data.

5.3. Recommendations

Near-real-time access to critical remote sensing data is essential for rapid characterization of eruptions by observatory scientists and academic partners. It could also allow for broader automated-detection development and implementation. With improved detection from passive instruments, we could better rapid-task others. Each generation of satellites launched and the subsequent increase in temporal and spatial resolution has proven valuable and motivates continued efforts to improve spatio-temporal resolution (e.g., forthcoming Landsat 9). In the Ulawun case, regional infrasound observations provided vastly more information than the remote observations. Adding regional infrasound stations has improved eruption detection capabilities in areas such as Alaska (Cameron et al., 2018), Chile (Matoza et al., 2018), and Southeast Asia (Taisne et al., 2019). Sharing and automating data processing codes has and will continue to improve our ability to detect and characterize eruptions. Part of our workflow made use of several open access software codes. Lightning continues to show promise as an eruption detection tool as the emitted electromagnetic radiation travels at the speed of light, but further work is needed to determine exactly what lightning indicates during an eruption. Combining lightning, infrasound, and satellite data was critical for the characterization of both the Raikoke and Ulawun eruptions, which suggests combining these tools for automated detection confirmation or satellite tasking would be powerful. For example, lightning detections followed by infrasound detections would provide confirmation of an eruption and could be used to automatically task an ASTER acquisition.

6. Conclusions

Fundamental and applied volcanological research are necessarily deeply intertwined. Physical and chemical observations further our fundamental understanding and provide insight into ongoing volcanic processes that inform monitoring and mitigation efforts. Conversely, monitoring efforts provide new observations and technologies that challenge and refine our understanding of how volcanoes work. This interplay highlights the power of academia and observatory collaboration, motivates retrospective characterization of eruptions, and ultimately advances both research and monitoring efforts. We retrospectively characterized the June 2019 eruption of Ulawun volcano using remote technologies: infrasound, lightning, and satellite remote sensing. Through our analyses we determined the latest eruption onset and earliest eruption cessation times, constrained *syn*-eruptive activity, and showed that eruptions may start with an explosive gas phase. We showed, as we did at Raikoke (McKee et al., 2021), that the strongest lightning strokes occur closer to the vent and lightning locations track plume development in that the strokes remain centralized with Ulawun's more symmetrical umbrella cloud. Our analyses also demonstrate that while remote observational tools are particularly good at constraining syn-eruptive activity at two VEI 4 eruptions, current technologies are limited in detecting pre-eruptive unrest. Ultimately, we further illustrated the power of combining remote observations to characterize volcanic eruptions.

Data access

Local radiosonde and ERA-Interim reanalysis modelled data available at http://weather.uwyo.edu/. Both ASTER and MODIS data are openly available at several locations online including NASA Earthdata Search (https://search.earthdata.nasa.gov/search) and the USGS EarthExplorer (https://earthexplorer.usgs.gov/). All Sentinel-2 data we use in this study are openly available at the Sentinel-hub EO-Browser (https://www.sentinel-hub.com/explore/eobrowser). GLD360 data are available from Vaisala Inc. through request. Data from the CTBT IMS infrasound network are available through the CTBTO vDEC platform (https://www. ctbto.org/specials/vdec/).

Declaration of Competing Interest

The authors declare that they have no known competing financial interests or personal relationships that could have appeared to influence the work reported in this paper.

Acknowledgments

This project originated at the Cooperative Institute for Dynamic Earth Research (CIDER) 2019 Summer Program: Volcanoes funded by NSF Grant EAR-1664595 to Bruce Buffett, Barbara Romanowicz, Roland Burgmann, Michael Manga, and Richard Allen. We thank two anonymous reviewers and Dave Schneider for helpful comments. McKee acknowledges NSF grant EAR-PF-1725730. Maher, de Negri, and Matoza acknowledge NSF grants EAR-1620576 and EAR-1847736. Smith acknowledges NSF grant EAR-PF-1855153. Carn acknowledges NASA grants 80NSSC17K0240 and 80NSSC20K0983. We used the following open access tools: UAFGeoTools (https://github.com/uafgeotools), ObsPy (https://github.com/obspy). This work comprises Earth Observatory of Singapore contribution no. 358. Disclaimer: The views presented in this work are those of the authors and do not necessarily represent the views of the CTBTO. Any use of trade, firm, or product names is for

descriptive purposes only and does not imply endorsement by the U.S. Government.

Appendix A. Supplementary data

Supplementary data to this article can be found online at https://doi.org/10.1016/j.jvolgeores.2021.107381.

References

Arason, P., Bennett, A.J., Burgin, L.E., 2011. Charge mechanism of volcanic lightning revealed during the 2010 eruption of Eyjafjallajökull. J. Geophys. Res. 116, 5315–5355. https://doi.org/10.1029/2011JB008651.

Bedard Jr., A.J., Georges, T.M., 2000. Atmospheric infrasound. Phys. Today 28, 32–37.

Behnke, S.A., McNutt, S.R., 2014. Using lightning observations as a volcanic eruption monitoring tool. Bull. Volcanol. 76, 112–193. https://doi.org/10.1007/s00445-014-0847-1.

Berrisford, P., Dee, D., Poli, P., Brugge, R., Fielding, K., Fuentes, M., Kallberg, P., Kobayashi, S., Uppala, S., Simmons, A., 2011. The ERA-Interim Archive, version 2.0.

Bishop, J.W., Fee, D., Szuberla, C.A.L., 2020. Improved infrasound array processing with robust estimators. Geophys. J. Int. 221, 2058. https://doi.org/10.1093/gji/ggaa110.

Brown, D., Ceranna, L., Prior, M., Mialle, P., Le Bras, R.J., 2014. The IDC seismic, hydroacoustic and infrasound global low and high noise models. Pure Appl. Geophys. 171, 361–375. https://doi.org/10.1007/s00024-012-0573-6.

Bursik, M., 2001. Effect of wind on the rise height of volcanic plumes. Geophys. Res. Lett. 28, 3621–3624. https://doi.org/10.1029/2001GL013393.

Cameron, C.E., Prejean, S.G., Coombs, M.L., Wallace, K.L., Power, J.A., Roman, D.C., 2018. Alaska volcano observatory alert and forecasting timeliness: 1989–2017. Front. Earth Sci. 6, 316–373. https://doi.org/10.3389/feart.2018.00086.

Cao, C., Xiong, J., Blonski, S., Liu, Q., Uprety, S., Shao, X., Bai, Y., Weng, F., 2013. Suomi NPP VIIRS sensor data record verification, validation, and long-term performance monitoring. J. Geophys. Res. Atmos. 118 (11), 664–11,678. https://doi.org/10.1002/2013JD020418.

Cao, C., De Luccia, F.J., Xiong, X., Wolfe, R., Weng, F., 2014. Early on-orbit performance of the visible infrared imaging radiometer suite onboard the Suomi National Polar-Orbiting Partnership (S-NPP) satellite. IEEE Trans. Geosci. Remote Sens. 52, 1142–1156. https://doi.org/10.1109/TGRS.2013.2247768.

Carlson, T.N., Ripley, D.A., 1997. On the relation between NDVI, fractional vegetation cover, and leaf area index. Remote Sens. Environ. 62, 241–252. https://doi.org/10.1016/S0034-4257(97)00104-1.

Carn, S.A., Krueger, A.J., Bluth, G.J.S., Schaefer, S.J., Krotkov, N.A., Watson, I.M., Datta, S., 2003. Volcanic eruption detection by the Total Ozone Mapping Spectrometer (TOMS) instruments: a 22-year record of Sulphur dioxide and ash emissions. Geol. Soc. Lond. Spec. Publ. 213, 177–202. https://doi.org/10.1144/GSL.SP.2003.213.01.11.

Carn, S.A., Krotkov, N.A., Yang, K., Krueger, A.J., 2013. Measuring Global Volcanic Degassing with the Ozone Monitoring Instrument (OMI). https://doi.org/10.1144/SP380.12.

Carn, S.A., Clarisse, L., Prata, A.J., 2016. Multi-decadal satellite measurements of global volcanic degassing. J. Volcanol. Geotherm. Res. 311, 99–134. https://doi.org/10.1016/j.jvolgeores.2016.01.002.

Carn, S.A., Fioletov, V.E., Mclinden, C.A., Li, C., Krotkov, N.A., 2017. A decade of global volcanic SO_2 emissions measured from space. Sci. Rep. 7, 1–12. https://doi.org/10.1038/srep44095.

Ceranna, L., Matoza, R., Hupe, P., Pichon, A.L., Landès, M., 2019. Infrasound Monitoring for Atmospheric Studies, Infrasound Monitoring for Atmospheric Studies. Springer International Publishing https://doi.org/10.1007/978-3-319-75140-5.

Chaussard, E., Amelung, F., Aoki, Y., 2013. Characterization of open and closed volcanic systems in Indonesia and Mexico using InSAR time series. J. Geophys. Res. Solid Earth 118, 3957–3969. https://doi.org/10.1002/jgrb.50288.

Christie, D.R., Campus, P., 2010. The IMS infrasound network: design and establishment of infrasound stations. Infrasound Monitoring for Atmospheric Studies. Springer Netherlands, Dordrecht, pp. 29–75 https://doi.org/10.1007/978-1-4020-9508-5_2.

Dee, D.P., Uppala, S.M., Simmons, A.J., Berrisford, P., Poli, P., Kobayashi, S., Andrae, U., Balmaseda, M.A., Balsamo, G., Bauer, P., Bechtold, P., Beljaars, A.C.M., van de Berg, L., Bidlot, J., Bormann, N., Delsol, C., Dragani, R., Fuentes, M., Geer, A.J., Haimberger, L., Healy, S.B., Hersbach, H., Hólm, E.V., Isaksen, L., Kaallberg, P., Köhler, M., Matricardi, M., McNally, A.P., Monge-Sanz, B.M., Morcrette, J.-J., Park, B.-K., Peubey, C., de Rosnay, P., Tavolato, C., Thépaut, J.-N., Vitart, F., 2011. The ERA-Interim reanalysis: configuration and performance of the data assimilation system. Q. J. R. Meteorol. Soc. 137, 553–597. https://doi.org/10.1002/qj.828.

Degruyter, W., Bonadonna, C., 2012. Improving on mass flow rate estimates of volcanic eruptions. Geophys. Res. Lett. 39. https://doi.org/10.1029/2012GL052566.

Ebmeier, S.K., Biggs, J., Mather, T.A., Amelung, F., 2013. On the lack of InSAR observations of magmatic deformation at Central American volcanoes. J. Geophys. Res. Solid Earth 118, 2571–2585.

Fedotov, S.A., 1985. Estimates of heat and pyroclast discharge by volcanic eruptions based upon the eruption cloud and steady plume observations. J. Geodyn. Geophysics and Volcanism 3, 275–302. https://doi.org/10.1016/0264-3707(85)90039–0.

Fee, D., Matoza, R.S., 2013. An overview of volcano infrasound: from hawaiian to plinian, local to global. J. Volcanol. Geotherm. Res. 249, 123–139. https://doi.org/10.1016/j.jvolgeores.2012.09.002.

Fee, D., Steffke, A., Garcés, M., 2010. Characterization of the 2008 Kasatochi and Okmok eruptions using remote infrasound arrays. J. Geophys. Res. 115, D00L10–D00L15. https://doi.org/10.1029/2009jd013621.

Fee, D., McNutt, S.R., Lopez, T.M., Arnoult, K.M., Szuberla, C.A.L., Olson, J.V., 2013. Combining local and remote infrasound recordings from the 2009 Redoubt Volcano eruption. J. Volcanol. Geotherm. Res. 259, 100–114. https://doi.org/10.1016/j.jvolgeores.2011.09.012.

Fee, D., Haney, M.M., Matoza, R.S., Van Eaton, A.R., Cervelli, P., Schneider, D.J., Iezzi, A.M., 2017. Volcanic tremor and plume height hysteresis from Pavlof Volcano, Alaska. Science 355, 45–48. https://doi.org/10.1126/science.aah6108.

Forward, K.M., Lacks, D.J., Sankaran, R.M., 2009. Charge segregation depends on particle size in triboelectrically charged granular materials. Phys. Rev. Lett. 102, 028001. https://doi.org/10.1103/PhysRevLett.102.028001.

Glaze, L.S., Baloga, S.M., Wilson, L., 1997. Transport of atmospheric water vapor by volcanic eruption columns. J. Geophys. Res. Atmos. 102, 6099–6108. https://doi.org/10.1029/96JD03125.

Global Volcanism Program, 1978. Report on Ulawun (Papua New Guinea). In: Squires, D. (Ed.), Scientific Event Alert Network Bulletin. vol. 3. Smithsonian Institution, p. 5. https://doi.org/10.5479/si.GVP.SEAN197805-252120.

Global Volcanism Program, 1983. Report on Ulawun (Papua New Guinea) (No. 9), Scientific Event Alert Network Bulletin, Scientific Event Alert Network Bulletin. Smithsonian Institution https://doi.org/10.5479/si.GVP.SEAN198309-252120.

Global Volcanism Program, 1989. Report on Ulawun (Papua New Guinea). In: McClelland, L. (Ed.), Scientific Event Alert Network Bulletin. 14. Smithsonian Institution, p. 1. https://doi.org/10.5479/si.GVP.SEAN198901-252120.

Global Volcanism Program, 2000. Report on Ulawun (Papua New Guinea). In: Wunderman, R. (Ed.), Bulletin of the Global Volcanism Network, 25:8. Smithsonian Institution https://doi.org/10.5479/si.GVP.BGVN200008-252120.

Global Volcanism Program, 2013. In: Venzke, E. (Ed.), Ulawun (252120) in Volcanoes of the World, v. 4.8.2. Smithsonian Institution Downloaded 20 Aug 2019.

Global Volcanism Program, 2019. Report on Ulawun (Papua New Guinea). In: Sennert, S.K. (Ed.), Weekly Volcanic Activity Report, 2 October–8 October 2019. Smithsonian Institution and U.S. Geological Survey . https://volcano.si.edu/showreport.cfm?doi=GVP.WVAR20191002-252120.

Hargie, K.A., Van Eaton, A.R., Mastin, L.G., Holzworth, R.H., Ewert, J.W., Pavolonis, M., 2019. Globally detected volcanic lightning and umbrella dynamics during the 2014 eruption of Kelud, Indonesia. J. Volcanol. Geotherm. Res. 382, 81–91. https://doi.org/10.1016/j.jvolgeores.2018.10.016.

Hédervári, P., 1963. On the energy and magnitude of volcanic eruptions. Bull. Volcanol. 25, 373–385. https://doi.org/10.1007/BF02596568.

Houghton, I.M.P., Aplin, K.L., Nicoll, K.A., 2013. Triboelectric charging of volcanic ash from the 2011 Grímsvötn eruption. Phys. Rev. Lett. 111, 118501. https://doi.org/10.1103/PhysRevLett.111.118501.

James, M.R., Lane, S.J., Gilbert, J.S., 2000. Volcanic plume electrification: experimental investigation of a fracture-charging mechanism. J. Geophys. Res. Solid Earth 105, 16641–16649. https://doi.org/10.1029/2000JB900068.

James, M.R., Wilson, L., Lane, S.J., Gilbert, J.S., Mather, T.A., Harrison, R.G., Martin, R.S., 2008. Electrical charging of volcanic plumes. Space Sci. Rev. 137, 399–418.

Johnson, J.B., Ruiz, M.C., Ortiz, H.D., Watson, L.M., Viracucha, G., Ramon, P., Almeida, M., 2018. Infrasound Tornillos produced by Volcán Cotopaxi's deep crater. Geophys. Res. Lett. 45, 5436–5444. https://doi.org/10.1029/2018GL077766.

Lee, D.-C., Olson, J.V., Szuberla, C.A.L., 2013. Computationally robust and noise resistant numerical detector for the detection of atmospheric infrasound. J. Acoust. Soc. Am. 134, 862–868. https://doi.org/10.1121/1.4807802.

Manley, G.F., Pyle, D.M., Mather, T.A., Rodgers, M., Clifton, D.A., Stokell, B.G., Thompson, G., Londoño, J.M., Roman, D.C., 2020. Understanding the timing of eruption end using a machine learning approach to classification of seismic time series. J. Volcanol. Geotherm. Res. 13, 106917. https://doi.org/10.1016/j.jvolgeores.2020.106917.

Marchetti, E., Ripepe, M., Harris, A.J.L., Delle Donne, D., 2009. Tracing the differences between Vulcanian and Strombolian explosions using infrasonic and thermal radiation energy. Earth Planet. Sci. Lett. 279, 273–281. https://doi.org/10.1016/j.epsl.2009.01.004.

Massimetti, F., Coppola, D., Laiolo, M., Valade, S., Cigolini, C., Ripepe, M., 2020. Volcanic hot-spot detection using SENTINEL-2: a comparison with MODIS–MIROVA thermal data series. Remote Sens. 12, 820. https://doi.org/10.3390/rs12050820.

Mastin, L.G., 2007. A user-friendly one-dimensional model for wet volcanic plumes. Geochem. Geophys. Geosyst. 8. https://doi.org/10.1029/2006GC001455.

Mastin, L.G., 2014. Testing the accuracy of a 1-D volcanic plume model in estimating mass eruption rate. J. Geophys. Res. Atmos. 119, 2474–2495. https://doi.org/10.1002/2013JD020604.

Matoza, R., Fee, D., Green, D., Mialle, P., 2019. Volcano infrasound and the international monitoring system. In: Le Pichon, A., Blanc, E., Hauchecorne, A. (Eds.), Infrasound Monitoring for Atmospheric Studies. Springer International Publishing, Cham, pp. 1023–1077 https://doi.org/10.1007/978-3-319-75140-5_33.

Matoza, R.S., Fee, D., Garcés, M.A., Seiner, J.M., Ramón, P.A., Hedlin, M.A.H., 2009. Infrasonic jet noise from volcanic eruptions. Geophys. Res. Lett. 36, L08303. https://doi.org/10.1029/2008GL036486.

Matoza, R.S., Landès, M., Le Pichon, A., Ceranna, L., Brown, D., 2013. Coherent ambient infrasound recorded by the International Monitoring System. Geophys. Res. Lett. 40, 429–433. https://doi.org/10.1029/2012GL054329.

Matoza, R.S., Fee, D., Le Pichon, A., Vergoz, J., Haney, M.M., Mikesell, T.D., Franco, L., Valderrama, O.A., Kelley, M.R., McKee, K., Ceranna, L., 2018. Local, regional, and remote seismo-acoustic observations of the April 2015 VEI 4 Eruption of Calbuco Volcano, Chile. J. Geophys. Res. Solid Earth 123, 3814–3827. https://doi.org/10.1002/2017JB015182.

McKee, K., Smith, C., Reath, K., Snee, E., Maher, S., Matoza, R.S., Carn, S., Mastin, L., Anderson, K., Damby, D., Roman, D., Degterev, A., Rybin, A., Chibisova, M., Assink, J., de Negri Leiva, R., Perttu, A., 2021. Evaluating the state-of-the-art in remote volcanic eruption characterization Part I: Raikoke volcano, Kuril Islands. J. Volcanol. Geotherm. Res., 107354 https://doi.org/10.1016/j.jvolgeores.2021.107354.

McNutt, S.R., Williams, E.R., 2010. Volcanic lightning: global observations and constraints on source mechanisms. Bull. Volcanol. 72, 1153–1167. https://doi.org/10.1007/s00445-010-0393-4.

Méndez Harper, J., Dufek, J., 2016. The effects of dynamics on the triboelectrification of volcanic ash. J. Geophys. Res. 121, 8209–8228. https://doi.org/10.1002/2015JD024275.

Morton, B.R., Taylor, G.I., Turner, J.S., 1956. Turbulent gravitational convection from maintained and instantaneous sources. Proc. R. Soc. Lond. Ser. Math. Phys. Sci. 234, 1–23. https://doi.org/10.1098/rspa.1956.0011.

National Academies of Sciences, Engineering, Medicine, 2020. A Vision for NSF Earth Sciences 2020–2030: Earth in Time. National Academies Press, Washington, D.C https://doi.org/10.17226/25761.

Newhall, C.G., Self, S., 1982. The volcanic explosivity index (VEI) an estimate of explosive magnitude for historical volcanism. J. Geophys. Res. 87, 1231. https://doi.org/10.1029/JC087iC02p01231.

Olson, J.V., Szuberla, C.A., 2008. Processing infrasonic array data. In: Havelock, D., Kuwano, S., Vorlander, M. (Eds.), Handbook of Signal Processing in Acoustics. Springer, New York, NY, pp. 1487–1496.

den Ouden, O.F., Assink, J.D., Smets, P.S., Shani-Kadmiel, S., Averbuch, G., Evers, L.G., 2020. CLEAN beamforming for the enhanced detection of multiple infrasonic sources. Geophys. J. Int. 221, 305–317. https://doi.org/10.1093/gji/ggaa010.

Pavolonis, M.J., Sieglaff, J., Cintineo, J., 2018. Automated Detection of Explosive Volcanic Eruptions Using Satellite-Derived Cloud Vertical Growth Rates. Earth Space Sci. 5, 903–928. https://doi.org/10.1029/2018EA000410.

Perttu, A., Caudron, C., Assink, J.D., Metz, D., Tailpied, D., Perttu, B., Hibert, C., Nurfiani, D., Pilger, C., Muzli, M., Fee, D., Andersen, O.L., Taisne, B., 2020. Reconstruction of the 2018 tsunamigenic flank collapse and eruptive activity at Anak Krakatau based on eyewitness reports, seismo-acoustic and satellite observations. Earth Planet. Sci. Lett. 541, 116268. https://doi.org/10.1016/j.epsl.2020.116268.

Phillipson, G., Sobradelo, R., Gottsmann, J., 2013. Global volcanic unrest in the 21st century: an analysis of the first decade. J. Volcanol. Geotherm. Res. 264, 183–196. https://doi.org/10.1016/j.jvolgeores.2013.08.004.

Planet Team, 2017. Planet Application Program Interface: In Space for Life on Earth. (San Francisco, CA) https://api.planet.com.

Poland, M.P., Lopez, T., Wright, R., Pavolonis, M.J., 2020. Forecasting, detecting, and tracking volcanic eruptions from space. Remote Sens. Earth Syst. Sci. 3, 55–94. https://doi.org/10.1007/s41976-020-00034-x.

Posmentier, E.S., 1967. A theory of microbaroms. Geophys. J. Int. 13, 487–501.

Prata, A.J., Grant, I.F., 2001. Retrieval of microphysical and morphological properties of volcanic ash plumes from satellite data: application to Mt Ruapehu, New Zealand. Q. J. R. Meteorol. Soc. 127, 2153–2179. https://doi.org/10.1002/qj.49712757615.

Prata, A.J., Gangale, G., Clarisse, L., Karagulian, F., 2010. Ash and sulfur dioxide in the 2008 eruptions of Okmok and Kasatochi: Insights from high spectral resolution satellite measurements. J. Geophys. Res. Atmos. 115. https://doi.org/10.1029/2009JD013556.

Prata, A.T., Folch, A., Prata, A.J., Biondi, R., Brenot, H., Cimarelli, C., Corradini, S., Lapierre, J., Costa, A., 2020. Anak Krakatau triggers volcanic freezer in the upper troposphere. Sci. Rep. 10, 3584. https://doi.org/10.1038/s41598-020-60465-w.

Pyle, D.M., 1989. The thickness, volume and grainsize of tephra fall deposits. Bull. Volcanol. 51, 1–15. https://doi.org/10.1007/BF01086757.

Pyle, D.M., 1995. Mass and energy budgets of explosive volcanic eruptions. Geophys. Res. Lett. 22, 563–566. https://doi.org/10.1029/95GL00052.

Pyle, D.M., 2015. Sizes of Volcanic Eruptions, Second editio, The Encyclopedia of Volcanoes. Elsevier Inc https://doi.org/10.1016/b978-0-12-385938-9.00013-4.

Reath, K., Pritchard, M., Poland, M., Delgado, F., Carn, S., Coppola, D., Andrews, B., Ebmeier, S.K., Rumpf, E., Henderson, S., Baker, S., Lundgren, P., Wright, R., Biggs, J., Lopez, T., Wauthier, C., Moruzzi, S., Alcott, A., Wessels, R., Griswold, J., Ogburn, S., Loughlin, S., Meyer, F., Vaughan, G., Bagnardi, M., 2019a. Thermal, deformation, and degassing remote sensing time series (CE 2000–2017) at the 47 most active volcanoes in Latin America: implications for volcanic systems. J. Geophys. Res. Solid Earth 124, 195–218. https://doi.org/10.1029/2018JB016199.

Reath, K., Pritchard, M.E., Moruzzi, S., Alcott, A., Coppola, D., Pieri, D., 2019b. The AVTOD (ASTER Volcanic thermal output database) Latin America archive. J. Volcanol. Geotherm. Res. 376, 62–74. https://doi.org/10.1016/j.jvolgeores.2019.03.019.

Riedel, K.S., Sidorenko, A., 1995. Minimum bias multiple taper spectral estimation. IEEE Trans. Signal Process. 43, 188–195. https://doi.org/10.1109/78.365298.

Rodgers, M., Roman, D.C., Geirsson, H., LaFemina, P., Muñoz, A., Guzman, C., Tenorio, V., 2013. Seismicity accompanying the 1999 eruptive episode at Telica Volcano, Nicaragua. J. Volcanol. Geotherm. Res. 265, 39–51. https://doi.org/10.1016/j.jvolgeores.2013.08.010.

Roman, D.C., LaFemina, P.C., Bussard, R., Stephens, K., Wauthier, C., Higgins, M., Feineman, M., Arellano, S., de Moor, J.M., Avard, G., Cruz, M.M., Burton, M., Varnam, M., Saballos, A., Ibarra, M., Strauch, W., Tenorio, V., 2019. Mechanisms of unrest and eruption at persistently restless volcanoes: insights from the 2015 Eruption of Telica Volcano, Nicaragua. Geochem. Geophys. Geosyst. 20, 4162–4183. https://doi.org/10.1029/2019GC008450.

Said, R.K., Inan, U.S., Cummins, K.L., 2010. Long-range lightning geolocation using a VLF radio atmospheric waveform bank. J. Geophys. Res. 115, D05208–D05219. https://doi.org/10.1029/2010JD013863.

Said, R., Murphy, M., 2016. GLD360 upgrade: performance analysis and applications. Presented at the 24th International Lightning Detection Conference & 6th International Lightning Meteorology Conference. San Diego, CA, p. 8.

Schneider, D.J., Hoblitt, R.P., 2013. Doppler weather radar observations of the 2009 eruption of Redoubt Volcano, Alaska. J. Volcanol. Geotherm. Res. 259, 133–144.

Scollo, S., Kahn, R.A., Nelson, D.L., Coltelli, M., Diner, D.J., Garay, M.J., Realmuto, V.J., 2012. MISR observations of Etna volcanic plumes. J. Geophys. Res. 117.

Silver, E., Day, S., Ward, S., Hoffmann, G., Llanes, P., Driscoll, N., Appelgate, B., Saunders, S., 2009. Volcano collapse and tsunami generation in the Bismarck Volcanic Arc, Papua New Guinea. J. Volcanol. Geotherm. Res. 186, 210–222. https://doi.org/10.1016/j.jvolgeores.2009.06.013.

Stall, S., Yarmey, L., Boehm, R., Cousijn, H., Cruse, P., Cutcher-Gershenfeld, J., Dasler, R., de Waard, A., Duerr, R., Elger, K., Fenner, M., Glaves, H., Hanson, B., Hausman, J., Heber, J., Hills, D., Hoebelheinrich, N., Hou, S., Kinkade, D., Koskela, R., Martin, R., Lehnert, K., Murphy, F., Nosek, B., Parsons, M., Petters, J., Plante, R., Robinson, E., Samors, R., Servilla, M., Ulrich, R., Witt, M., Wyborn, L., 2018. Advancing FAIR data in earth, space, and environmental science. Eos 99. https://doi.org/10.1029/2018EO109301.

Taisne, B., Perttu, A., Tailpied, D., Caudron, C., Simonini, L., 2019. Atmospheric controls on ground- and space-based remote detection of volcanic ash injection into the atmosphere, and link to early warning systems for aviation hazard mitigation. In: Le Pichon, A., Blanc, E., Hauchecorne, A. (Eds.), Infrasound Monitoring for Atmospheric Studies: Challenges in Middle Atmosphere Dynamics and Societal Benefits. Springer International Publishing, Cham, pp. 1079–1105 https://doi.org/10.1007/978-3-319-75140-5_34.

Theys, N., Smedt, I.D., Yu, H., Danckaert, T., van Gent, J., Hörmann, C., Wagner, T., Hedelt, P., Bauer, H., Romahn, F., 2017. Sulfur dioxide retrievals from TROPOMI onboard Sentinel-5 Precursor: algorithm theoretical basis. Atmospheric Meas. Tech. 10.

Tsuya, H., 1955. Geological and Petrological Studies of Volcano, Fuji, V. : 5. On the 1707 eruption of Volcano Fuji. Bull Earthq Res Inst 33, 341–383.

Van Eaton, A.R., Schneider, D.J., Smith, C.M., Haney, M.M., Lyons, J.J., Said, R., Fee, D., Holzworth, R.H., Mastin, L.G., 2020. Did ice-charging generate volcanic lightning during the 2016–2017 eruption of Bogoslof volcano, Alaska? Bull. Volcanol. 82. https://doi.org/10.1007/s00445-019-1350-5.

Walker, G.P.L., 1973. Explosive volcanic eruptions — a new classification scheme. Geol. Rundsch. 62, 431–446. https://doi.org/10.1007/BF01840108.

Wallace, L.M., Stevens, C., Silver, E., McCaffrey, R., Loratung, W., Hasiata, S., Stanaway, R., Curley, R., Rosa, R., Taugaloidi, J., 2004. GPS and seismological constraints on active tectonics and arc-continent collision in Papua New Guinea: implications for mechanics of microplate rotations in a plate boundary zone. J. Geophys. Res. Solid Earth 109, 1–16. https://doi.org/10.1029/2003JB002481.

Wilkinson, M.D., Dumontier, M., Aalbersberg, Ij.J., Appleton, G., Axton, M., Baak, A., Blomberg, N., Boiten, J.-W., da Silva Santos, L.B., Bourne, P.E., Bouwman, J., Brookes, A.J., Clark, T., Crosas, M., Dillo, I., Dumon, O., Edmunds, S., Evelo, C.T., Finkers, R., Gonzalez-Beltran, A., Gray, A.J.G., Groth, P., Goble, C., Grethe, J.S., Heringa, J., Hoen, P.A.C., Hooft, R., Kuhn, T., Kok, R., Kok, J., Lusher, S.J., Martone, M.E., Mons, A., Packer, A.L., Persson, B., Rocca-Serra, P., Roos, M., van Schaik, R., Sansone, S.-A., Schultes, E., Sengstag, T., Slater, T., Strawn, G., Swertz, M.A., Thompson, M., van der Lei, J., van Mulligen, E., Velterop, J., Waagmeester, A., Wittenburg, P., Wolstencroft, K., Zhao, J., Mons, B., 2016. The FAIR guiding principles for scientific data management and stewardship. Sci. Data 3, 160018. https://doi.org/10.1038/sdata.2016.18.

Williams, E., Nathou, N., Hicks, E., Pontikis, C., Russell, B., Miller, M., Bartholomew, M.J., 2009. The electrification of dust-lofting gust fronts ('haboobs') in the Sahel. Atmos. Res. 91, 292–298. https://doi.org/10.1016/j.atmosres.2008.05.017.

Wilson, C.R., Olson, J.V., Osborne, D.L., Le Pichon, A., 2003. Infrasound from Erebus volcano at I55US in Antarctica. Inframatics 4, 1–8.

Woods, A.W., 1993. A model of the plumes above basaltic fissure eruptions. Geophys. Res. Lett. 20, 1115–1118. https://doi.org/10.1029/93GL01215.

Wright, R., Flynn, L.P., Garbeil, H., Harris, A.J.L., Pilger, E., 2004. MODVOLC: near-real-time thermal monitoring of global volcanism. J. Volcanol. Geotherm. Res. 135, 29–49. https://doi.org/10.1016/j.jvolgeores.2003.12.008.

Yamaguchi, Y., Kahle, A.B., Tsu, H., Kawakami, T., Pniel, M., 1998. Overview of advanced spaceborne thermal emission and reflection radiometer (ASTER). IEEE Trans. Geosci. Remote Sens. 36, 1062–1071. https://doi.org/10.1109/36.700991.